



Pollution trace gases C₂H₆, C₂H₂, HCOOH, and PAN in the North Atlantic UTLS: observations and simulations

Gerald Wetzel¹, Felix Friedl-Vallon¹, Norbert Glatthor¹, Jens-Uwe Groöß²,
Thomas Gulde¹, Michael Höpfner¹, Sören Johansson¹, Farahnaz Khosrawi¹,
5 Oliver Kirner³, Anne Kleinert¹, Erik Kretschmer¹, Guido Maucher¹, Hans
Nordmeyer¹, Hermann Oelhaf¹, Johannes Orphal¹, Christof Piesch¹, Björn-Martin
Sinnhuber¹, Jörn Ungermann², and Bärbel Vogel²

¹Karlsruhe Institute of Technology, Institute of Meteorology and Climate Research, Karlsruhe, Germany

²Research centre Jülich, Institute of Energy and Climate Research – Stratosphere (IEK-7), Jülich, Germany

10 ³Karlsruhe Institute of Technology, Steinbuch Centre for Computing, Karlsruhe, Germany

Correspondence to: Gerald Wetzel (gerald.wetzel@kit.edu)

Abstract

Measurements of the pollution trace gases ethane (C₂H₆), ethyne (C₂H₂), formic acid
15 (HCOOH), and peroxyacetyl nitrate (PAN) were performed in the North Atlantic upper
troposphere and lowermost stratosphere (UTLS) region with the airborne limb imager GLORIA
(Gimballed Limb Observer for Radiance Imaging of the Atmosphere) with high spatial
resolution down to cloud top. Observations were made during flights with the German research
aircraft HALO (High Altitude and LOng Range Research Aircraft) in the frame of the WISE
20 (Wave-driven ISentropic Exchange) campaign, which was carried out in autumn 2017 from
Shannon (Ireland) and Oberpfaffenhofen (Germany). Enhanced volume mixing ratios (VMR)
of up to 2.2 ppbv C₂H₆, 0.2 ppbv C₂H₂, 0.9 ppbv HCOOH, and 0.4 ppbv PAN were detected
during the flight on 13 September 2017 in the upper troposphere and around the tropopause
above the British Isles. Since PAN has the longest lifetime of this foursome, elevated quantities
25 of this molecule could be measured even in the lowermost stratosphere (locally up to 14 km).
Backward trajectory calculations as well as global three-dimensional CLaMS simulations with
artificial tracers of air mass origin have shown that the main sources of the observed pollutant
species are forest fires in North America and anthropogenic pollution in South and Southeast
Asia uplifted and moved within the Asian monsoon anticyclone (AMA) circulation system.
30 After release from the AMA, these species or their precursor substances are transported by
strong tropospheric winds over large distances, depending on their particular atmospheric
lifetime of up to months. Observations are compared to simulations with the atmospheric



models EMAC (ECHAM5/MESy Atmospheric Chemistry) and CAMS (Copernicus
Atmosphere Monitoring Service). These models are qualitatively able to reproduce the
35 measured VMR enhancements but underestimate the absolute amount of the increase.
Increasing the emissions in EMAC by a factor of 2 reduces the disagreement between simulated
and measured results and illustrates the importance of the quality of emission databases used in
chemical models.

40 1 Introduction

Organic compounds in the troposphere like ethane, ethyne, formic acid, and secondary order
(not directly emitted) pollutants like peroxyacetyl nitrate are involved in many atmospheric
processes. These pollutants can be transported into remote regions due to their long lifetime
under appropriate atmospheric conditions, like convective processes combined with strong
45 wind regimes of the upper troposphere such as the subtropical jet stream (e.g., Lu et al., 2019;
Alvarado et al., 2020). At these altitudes, such hydrocarbons and nitrogen-containing
substances (like peroxyacetyl nitrate) may also influence the amount of ozone that is known to
be an effective greenhouse gas in the upper troposphere and lowermost stratosphere (UTLS)
region since it largely influences the radiation budget around the tropopause (Forster and Shine,
50 1997; Hansen et al., 1997; Xie et al., 2008; Riese et al., 2012).

Emissions of ethane (C_2H_6), the most important tropospheric non-methane hydrocarbon
(NMHC) species, are connected with biomass burning and natural gas losses (Rudolph, 1995;
Singh et al., 2001). The production of fossil fuels together with biofuel use also are important
sources of this molecule (Xiao et al., 2008). It is removed from the atmosphere by reaction with
55 the hydroxyl (OH) radical (Xiao et al., 2008). The mean lifetime of C_2H_6 is about two months
(Rudolph, 1995) such that C_2H_6 may be transported far away from its source regions.

The trace gas ethyne (C_2H_2) is emitted into the troposphere by combustion of biofuels and fossil
fuels, as well as biomass burning (Xiao et al., 2007). As in the case of C_2H_6 , the reaction with
the OH radical is also responsible for the loss of C_2H_2 in the atmosphere. The mean lifetime of
60 C_2H_2 is shorter compared to the one of C_2H_6 and amounts to about two weeks (Xiao et al.,
2007).

Formic acid (HCOOH) has many different sources. Direct emissions from plants, biomass
burning, and fossil fuel combustion are important factors producing this molecule (Mungall et



65 al., 2018). A secondary photochemical formation takes place from anthropogenic and biogenic precursors (Yuan et al., 2015) like oxidation of volatile organic compounds (Khare et al., 1999). The loss of HCOOH is possible due to wet and dry deposition as well as oxidation with the OH radical (Paulot et al., 2011). The atmospheric mean lifetime of HCOOH is very variable and ranges from one or two days in the boundary layer up to a few weeks in the free troposphere (Millet et al., 2015).

70 The molecule peroxyacetyl nitrate ($\text{CH}_3\text{COO}_2\text{NO}_2$), commonly named as PAN, is formed via a three-body-reaction of peroxyacetyl (CH_3COO_2) with nitrogen dioxide (NO_2) and a third partner M (mainly N_2 or O_2):



75 The reverse reaction of (R1) is the thermal decomposition of PAN and defines the main loss of this molecule in the atmosphere (Fischer et al., 2014) while photolysis becomes dominant in the UTLS region (Fadnavis et al., 2015). Two minor loss processes of PAN are reactions with OH and dry deposition (Fischer et al., 2014). The mean atmospheric lifetime of PAN is very variable since it is strongly dependent on the ambient temperature. While the mean lifetime amounts to only one hour at temperatures of 298 K, it rises up to a few months under cold upper
80 tropospheric conditions (Singh, 1987; Fischer et al., 2014). Hence, enhanced PAN amounts (which serve as an NO_2 reservoir) can be transported over wide geographical regions in the middle and upper troposphere. Thus, NO_2 released by the backward reaction of (R1) may contribute to an increase of tropospheric ozone far away from the PAN sources (Singh, 1987; Fadnavis et al., 2014; Ungermann et al., 2016).

85 Scientific flights of the airborne limb imager GLORIA (Gimballed Limb Observer for Radiance Imaging of the Atmosphere) were carried out aboard HALO (High Altitude and Long Range Research Aircraft) during the WISE (Wave-driven ISentropic Exchange) campaign in autumn 2017 above the North Atlantic. This atmospheric region is characterized by intense dynamical activity reflected in complex structures like tropopause folds and air masses of different origin.
90 Tropospheric pollutants like C_2H_6 , C_2H_2 , HCOOH, and PAN were observed together with stratospheric trace gases like O_3 in the UTLS region. A description of the GLORIA instrument, data analysis and chemical modelling is given in Sect. 2. A discussion of observed vertical volume mixing ratio (VMR) profiles of trace species follows in Sect. 3 together with a comparison of the measured data to simulations of the chemistry climate model EMAC
95 (ECHAM5/MESSy Atmospheric Chemistry) and to assimilated data of CAMS (Copernicus



Atmosphere Monitoring Service). A discussion on the possible origin of air masses at the Earth's boundary layer detected by GLORIA is also included in this section.

2 GLORIA instrument, data analysis and modelling

100 In the following subsections, we give an overview of the GLORIA instrument and the flights with the HALO aircraft, together with the corresponding data analysis and a description of atmospheric modelling performed for this study.

2.1 GLORIA instrument and HALO flights

The cryogenic Fourier Transform limb emission spectrometer GLORIA operates in the thermal
105 infrared spectral region between about 7 and 13 μm using a 2-dimensional detector array using 128 vertical and 48 horizontal interferograms per measurement (Friedl-Vallon et al., 2014; Riese et al., 2014). The interferograms are Fourier transformed into the spectral domain and radiometrically calibrated using in-flight measurements of two blackbodies (Kleinert et al., 2014). Furthermore, spectra in the horizontal direction were averaged to improve the signal to
110 noise ratio such that the noise equivalent spectral radiance (NESR) finally amounts to about $1.5 \times 10^{-8} \text{ W}(\text{cm}^2 \text{ sr cm}^{-1})^{-1}$. Spectra recorded with maximum optical path difference of 8.0 cm, which corresponds to an unapodized spectral resolution of 0.0625 cm^{-1} , were used for this study. These so-called chemistry mode spectra, are apodized with the Norton and Beer (1976) “strong”
115 function. Due to the high spectral resolution, these measurements allow the retrieval of many species with minor contribution to the spectra by the separation of individual spectral lines from continuum-like emissions.

In this study, we report results from the WISE aircraft campaign, which was dedicated mainly to the investigation of dynamical processes and the evolution of air masses within the context of stratosphere-troposphere exchange. Sixteen flights with HALO were performed from
120 Shannon (Ireland) and Oberpfaffenhofen (Germany) between 31 August 2017 and 21 October 2017, in a region within about 40° W and 15° E longitude and 40° N and 75° N latitude. In the following sections, we focus on results of the flight on 13 September 2017 where strong enhancements in the VMR of the pollutant species C_2H_6 , C_2H_2 , HCOOH , and PAN were observed by GLORIA. Figure 1 shows the flight path consisting of two main legs together with
125 tangent points of GLORIA where the instrument was operated in the chemistry mode.



2.2 Data analysis of measured spectra

Radiances are calculated with the Karlsruhe Optimized and Precise Radiative transfer Algorithm (KOPRA; Stiller et al., 2002) based on spectroscopic parameters from the high-resolution transmission molecular absorption database (HITRAN; Gordon et al., 2017). The retrieval itself is performed with the procedure KOPRAFIT (Höpfner et al., 2002) using derivatives of the radiance spectrum with respect to atmospheric state and instrument parameters (Jacobians) calculated by KOPRA. The inverse problem of radiative transport is solved by KOPRAFIT with a Gauss-Newton iterative method (Rodgers, 2000) in combination with a Tikhonov-Phillips regularization approach (Phillips, 1962; Tikhonov, 1963) using a constraint with respect to a first derivative of the a priori profile of the target species.

In a first step cloud affected spectra are filtered out using a cloud index as described in Spang et al. (2004). Spectra with a colour ratio of the mean radiance in two spectral windows ($788.20\text{--}796.25\text{ cm}^{-1}$ and $832.30\text{--}834.40\text{ cm}^{-1}$) larger than 2 were chosen for the retrieval process. Prior to the trace gas retrievals, the pointing elevation angle was retrieved to compensate for systematic misalignment of the line of sight (LOS) of the instrument according to the method described in Johansson et al. (2018). The final pointing (LOS) error was estimated to 0.01° . Vertical profiles of atmospheric species were taken from a climatological atmosphere (Remedios et al., 2007), updated with surface concentration data from NOAA ESRL GMD (National Oceanic and Atmospheric Administration, Earth System Research Laboratory, Global Monitoring Division; Montzka et al., 1999). Subsequently, a temperature retrieval was carried out using pressure-temperature a priori data from the European Centre for Medium-Range Weather Forecasts (ECMWF) which was interpolated to the GLORIA vertical retrieval grid. Spectral windows around 811 and 957 cm^{-1} containing appropriate CO_2 transitions were used for this analysis. The total error of the temperature retrieval calculations is estimated to about 1.5 K (Johansson et al., 2018).

The spectral analysis of the target species C_2H_6 , C_2H_2 , HCOOH , and PAN is impeded by overlapping features of so-called disturbing gases in the corresponding spectral region. Hence, a careful selection of appropriate microwindows is essential to perform retrievals with good accuracy. Test retrievals allowed to find microwindows with respect to little overlapping of spectral signatures of disturbing gases in combination with a high sensitivity of line intensities of target species with respect to changes in their concentration. Main interfering species were



either adjusted simultaneously together with the target molecule or pre-fitted in a different spectral interval.

The analysis of C_2H_6 was performed in four microwindows within the ν_9 band between 819 and 833 cm^{-1} (see Fig. 2a). Many overlapping features of so-called disturbing gases are visible in this spectral region, first of all H_2O and CO_2 . The error budget of C_2H_6 is shown in Fig. 2b. At higher altitudes with low C_2H_6 values, the total error of this molecule is dominated by the temperature error. Lower down in the VMR maximum region, the systematic spectroscopic error of C_2H_6 (as given in HITRAN) governs the error budget. The total error of C_2H_6 remains within about 15 % in the altitude region of the upper troposphere.

Retrieval calculations of C_2H_2 were carried out in the R-branch region of the ν_5 band. Figure 3a shows spectral contributions of relevant species in four microwindows between 759 and 781 cm^{-1} that have been found best appropriate to derive C_2H_2 from GLORIA spectra. The corresponding retrieval error budget of C_2H_2 is given in Fig. 3b. The random noise error is dominating the budget over nearly the complete altitude range. The total error of C_2H_2 stays within 10-15 % in the region of the VMR maximum in the upper troposphere.

The analysis of the molecule $HCOOH$ was performed in the spectral range between 1086 and 1117 cm^{-1} (see Fig. 4a). Three microwindows were chosen including the strong Q-branch of the $HCOOH$ ν_6 vibrational band. The spectral region is dominated by spectral features due to O_3 , CO_2 , CFC-12, and HCFC-22 transitions. The spectroscopic part of the total error is dominant in the altitude region of the $HCOOH$ VMR maximum in the upper troposphere (see Fig. 4b). Here, the total $HCOOH$ error stays within 10 %. Apart from this altitude region, the error budget is governed by the random noise part and the total error increases significantly (mainly in the upper part of the profile with low $HCOOH$ values).

The retrieval of PAN was conducted in two broad microwindows of the ν_{16} band between 780 and 805 cm^{-1} (see Fig. 5a). The spectral gap between these microwindows was chosen such that the strong CO_2 Q-branch at 792 cm^{-1} was excluded from the data analysis. Beside CO_2 , the molecules H_2O and CCl_4 are the main interfering species in the spectral region of PAN. The retrieval error budget is depicted in Fig. 5b. Beside random noise, further error sources like inaccuracies in the FOV and the retrieved temperature profile contribute to the total PAN error that remains within 10 % in altitude regions with enhanced PAN amounts.

Besides the retrieval of the above-mentioned pollutant gases, the tracer species ozone was also inferred from the recorded spectra. Many spectral ozone lines are available in the mid-infrared



spectral region. Transitions between 780 and 788 cm^{-1} within the ν_2 band were chosen for the
190 retrieval process similar to the method described in Johansson et al. (2018). The total ozone
error is within 10 % with a vertical resolution of 0.3 to 1.5 km.

The altitude resolution of all retrievals, calculated from the full width at half maximum of the
columns of the averaging kernel matrix, was used as an a posteriori quality filtering of the
retrieved data. Only vertical profile parts with an altitude resolution of better than 2 km were
195 finally used for the data interpretation.

2.3 Model simulations

2.3.1 EMAC

Retrieved vertical profiles of trace species are compared to a multi-year simulation of the
chemistry climate model ECHAM5/MESSy Atmospheric Chemistry (EMAC). This Eulerian
200 model includes submodels describing tropospheric and middle atmosphere processes (Jöckel
et al., 2010). The core model is the 5th generation European Centre Hamburg general circulation
model (ECHAM5; Roeckner et al., 2006) that is connected to the submodels using the interface
Modular Earth Submodel System (MESSy). For the present study we applied EMAC
(ECHAM5 version 5.3.02, MESSy version 2.53) with a spherical truncation of T106
205 (corresponding to a resolution of approximately 1.125 by 1.125 degrees in latitude and
longitude) with 90 hybrid pressure levels from the ground up to 0.01 hPa. Meteorological data
fields are specified using a Newtonian relaxation technique of the surface pressure and
prognostic variables below 1 hPa with the ECMWF reanalysis ERA-Interim (Dee et al., 2011).
The simulation was initialized on 1 May 2017 and includes a comprehensive chemistry setup
210 from the troposphere to the lower mesosphere. Rate constants of gas-phase reactions originate
from Atkinson et al. (2007) and Sander et al. (2011). Photochemical reactions of precursor
substances important for the build-up of the species PAN (Fischer et al., 2014) were integrated
into the model setup. For surface emissions of non-methane volatile organic compounds
(NMVOCs), a data set of the MACCcity emission inventory (MACC/CityZEN; Granier et al.,
215 2011) and ACCMIP (Atmospheric Chemistry and Climate Model Intercomparison Project;
Lamarque et al., 2013) was used. Anthropogenic emission sources from biomass burning,
agricultural waste burning, fossil fuels, ship, road and aircraft, as well as biogenic emissions
are considered. For the simulated year 2017, most recent available emissions of 2010 are
repeated. In addition to this EMAC standard run, a second model simulation (called EMAC_2)



220 was performed using NMVOC emissions enhanced by a factor of 2 as recommended by Monks
et al. (2018). The model output data were saved every 5 hours during the time period of the
GLORIA observations. The model output to the GLORIA measurements was interpolated in
time and space to the observation geolocations.

2.3.2 CAMS

225 The Copernicus Atmosphere Monitoring Service (CAMS) produced by ECMWF is a reanalysis
dataset that produces continuous data on atmospheric composition (Inness et al., 2019). The
Integrated Forecast System (IFS) of ECMWF was integrated to allow for the data assimilation
and modelling of aerosols, chemically reactive species and greenhouse gases. Apart from
assimilated ozone, no stratospheric chemistry is simulated by the model system. In this study,
230 CAMS reanalyses were used with a horizontal resolution of about 80 km. The vertical
resolution consists of 60 pressure levels up to 0.1 hPa. Three-dimensional model output fields
are available every 3 hours. Detailed information on the CAMS model architecture is given by
Inness et al. (2019). An evaluation study of CAMS using aircraft observations was carried out
by Wang et al. (2020). Biases of assimilated species like ozone are found to be less than 20%
235 whereas discrepancies for gases like C₂H₆ and PAN are generally larger.

3 Results and discussion

In this section, vertical profiles retrieved from GLORIA measurements during the WISE
campaign on 13 September 2017 over the North Atlantic region are shown. Observed GLORIA
240 chemistry mode data are compared to EMAC and CAMS simulation results. The possible origin
of air masses detected by GLORIA is also discussed.

3.1 GLORIA measurements

Retrieved volume mixing ratios of C₂H₆, C₂H₂, HCOOH, and PAN together with O₃ inferred
from limb emission spectra during the WISE flight on 13 September 2017 are displayed in Fig.
245 6. Ozone is a molecule with highest concentrations in the stratosphere (Brosseur and Solomon,
2005). Hence, it can be used as a tracer to diagnose detected air masses whether they are of
stratospheric or tropospheric origin. The general shape of O₃ VMR is strongly correlated with
the tropopause as shown in Fig. 6a. There are two regions where stratospheric air comes down
to about 7 km (around 14:45 UTC and around 16:50 UTC). Here, the tropopause layer reaches



250 these low altitudes in the form of a stratospheric intrusion, while at the beginning and the end
of the measurement phase the troposphere extends up to about 12 km. Trajectory calculations
have shown that due to a west-southwesterly mid- and upper tropospheric air flow in the region
of the flight path shown in Fig. 1, GLORIA has sounded virtually the same air mass twice
yielding to a kind of symmetry in the horizontal trace gas distribution before and after 16:10
255 UTC. Measured stratospheric ozone volume mixing ratios are within 0.1 and 0.8 ppmv. These
values are in line with other mid-latitude observations performed in this altitude range (e.g.,
Cortesi et al., 2007; Livesey et al., 2008).

Measured concentrations of the species C_2H_6 are shown in Fig. 6b. The VMR distribution of
 C_2H_6 is in parts anti-correlated to the one of ozone. Two regions of strong VMR enhancements
260 up to about 2.2 ppbv can be seen in the upper troposphere at the beginning and at the end of the
measurement period over the region south of Ireland and near the coastline of The Netherlands
and Belgium. In the stratosphere, no stronger enhanced C_2H_6 VMR levels are visible and values
remain below about 0.6 ppbv what can be confirmed by mid-latitude satellite measurements
(Rinsland et al., 2005; Glatthor et al., 2009; Wiegele et al., 2012).

265 The same picture is present in the vertical and horizontal distribution of C_2H_2 amounts (see Fig.
6c). Elevated volume mixing ratios of up to 0.2 ppbv in the upper troposphere are clearly visible
at the beginning and close to the end of the observation period. In the stratosphere, measured
 C_2H_2 values appear noisy and stay clearly below 0.1 ppbv most of the time. C_2H_2 VMR
measured by GLORIA lies within the range of satellite data obtained in the same altitude region
270 at mid-latitudes (Rinsland et al., 2005; Wiegele et al., 2012).

Measured HCOOH volume mixing ratios are depicted in Fig. 6d. As in the case of the
previously mentioned species C_2H_6 and C_2H_2 , large amounts of HCOOH are also visible at high
altitudes in the troposphere during early and late time of the GLORIA observations with values
up to 0.9 ppbv. In contrast, stratospheric HCOOH values are low and not higher than 0.1 ppbv.
275 These values are in accordance with space-borne mid-latitude observations in the altitude
regime considered here (Rinsland et al., 2006; Grutter et al., 2010).

The 2-dimensional cross section of PAN is shown in Fig. 6e. The distribution of VMR maxima
and minima is more structured compared to the one of the previously regarded pollution trace
gases. Increased amounts of PAN up to 0.4 ppbv are not only visible at the beginning and end
280 of the observation period in the upper troposphere but also in the lowermost stratosphere around
15:00 UTC, at altitudes of 7 to 8 km. Somewhat less enhanced quantities are noticeable near 14



km around 15:30 UTC. Elevated PAN amounts of comparable magnitude have also been detected in the UTLS region by space-borne instruments (Coheur et al., 2007; Wiegele et al., 2012; Ungermann et al., 2016). This different shape of VMR distribution might be explained
285 by very long lifetimes of PAN under cold UTLS conditions and by the fact that PAN is not emitted directly but dependent on the availability of precursor substances as described in Sect. 1.

3.2 Comparison to model simulations

The comparison of measured species to model simulations is presented in Figs. 7 and 8. The
290 observed data have been temporally smoothed with a 39-point adjacent averaging routine to permit a more realistic comparison with respect to different horizontal resolutions in the measurement and the EMAC and CAMS simulations. Concerning O₃, both simulations principally reproduce the tropospheric and stratospheric concentrations seen by GLORIA (see Fig. 7a-c) but with coarser spatial structure. The chemistry climate model EMAC is able to
295 simulate finer structures while CAMS only produces a smooth distribution of assimilated ozone. Both models tend to slightly overestimate the amount of ozone in the troposphere. This is also visible in Fig. 8a-c where differences between both EMAC runs (with and without enhanced NMVOC emissions) and GLORIA observations are shown. The amount of simulated ozone in the EMAC_2 run is only slightly higher (less than 10 ppbv) compared to the EMAC
300 simulation without enhanced NMVOC emissions (VMR differences in Fig. 8b and Fig. 8c are therefore nearly the same).

The comparison of C₂H₆ is displayed in Fig. 7d-f. Both models are able to qualitatively reproduce the temporal and spatial region of enhanced upper tropospheric C₂H₆ as observed by GLORIA. As in the case of ozone, EMAC again is able to display finer structures in the vertical
305 and horizontal distribution of C₂H₆ compared to CAMS. However, deficits in the simulated absolute C₂H₆ quantities are clearly visible in both models, especially in the case of CAMS. A considerable underestimation of CAMS C₂H₆ with respect to airborne observations was already reported by Wang et al. (2020). The EMAC_2 simulation with increased NMVOC emissions at least reduces the difference to the GLORIA observations compared to the EMAC run without
310 these stronger NMVOC emissions (see Fig. 8d-f).

Concerning the molecule C₂H₂, we recognize that EMAC generates elevated concentrations in the same upper tropospheric region as they are observed by GLORIA (see Fig. 7 g-h). In



315 addition, the measured VMRs in the upper troposphere are only little underestimated in terms of their absolute amount by the EMAC_2 simulation using raised NMVOC emissions. In the stratosphere, simulated C_2H_2 amounts are too low compared to the measurement. Using standard NMVOC emissions in EMAC leads to an increased underestimation of C_2H_2 amounts compared to GLORIA (see Fig. 8g-i).

320 The comparison of the species HCOOH is shown in Fig. 7i-k and Fig. 8j-l. Elevated HCOOH concentrations, as recorded by GLORIA in the upper troposphere, are clearly underestimated by both models, especially in the CAMS simulation, although the atmospheric region of the (too weak) enhanced HCOOH amounts in the models agrees with the measured one. However, the EMAC_2 simulation at least reduces differences with respect to the GLORIA observations.

Looking at the temporal and spatial distribution of PAN the situation appears somewhat different to the comparisons discussed above (see Fig. 7l-n and Fig. 8m-o). The principal 325 behaviour of enhanced PAN values in the upper troposphere is captured by both atmospheric models. EMAC produces slightly finer structures in the stratosphere compared to CAMS. However, the measured small scale variations in the amount of PAN especially near 14:30 UTC between 6 and 8 km are not reproduced by the EMAC_2 simulation with enhanced NMVOC emissions while the observed elevated PAN values around 15:00 UTC in the lowermost 330 stratosphere from 7 to 8 km are also visible in the model output. Apart from the regions with the highest measured PAN amounts, EMAC_2 tends to overestimate the concentration of PAN below about 13 km (what is not the case in the standard EMAC run). Interesting VMR variations are also seen by GLORIA in the stratosphere above 13 km. The PAN VMR maximum detected around 15:40 UTC near 14 km is not visible in the model simulations. The PAN VMR 335 minima near 15:00 UTC and between 16:00 UTC and 16:15 UTC at about 13.5 km are reflected as a VMR minimum in EMAC_2, although with lower absolute quantities. The different shape of the horizontal and vertical distribution of PAN VMR is most probably caused by long-range atmospheric transport. Compared to the species discussed before, sources and sinks are different, and atmospheric lifetime of PAN is considerably longer. In the following subsection, 340 we will focus on the origin of the polluted air masses, which have been detected by GLORIA.

3.3 Origin of polluted air masses

To estimate the geographical region (within the Earth's upper planetary boundary layer) of the origin of the measured enhanced amounts of the pollutants we performed backward trajectory



calculations as well as global three-dimensional CLaMS simulations with artificial tracers of
345 air mass origin as described in the following subsections.

3.3.1 CLaMS backward trajectory calculations

To obtain a more detailed insight into the origin and transport pathways of air masses, backward
trajectories with the three-dimensional Chemical Lagrangian Model of the Stratosphere
(CLaMS; McKenna et al., 2002b; McKenna et al., 2002a; Pommrich et al., 2014) were
350 performed starting from the GLORIA measurements. Although pure trajectories do not include
mixing processes, they are well suited to analyse the history of transport pathways of air parcels
in the tropics and in the region of the Asian monsoon into the UTLS (Vogel et al., 2014; Li et
al., 2018; Ploeger et al., 2012). In this study, 20-, 40-, and 60-days diabatic backward
trajectories with a horizontal resolution of 1 x 1 degrees were calculated using ERA-interim
355 reanalysis wind data (Dee et al., 2011).

These trajectories were generated for defined areas, where enhanced or low VMRs of pollutants
have been detected by GLORIA. Selected regions are displayed as coloured boxes in Fig. 6.
High amounts of pollutants are recorded within the cyan and blue boxes mainly in the upper
troposphere. Air masses marked in these two boxes are located near the stratospheric intrusion.
360 This region was probed twice, first at the beginning and second at the end of the flight (see Fig.
1). In addition, the green box marks enhanced quantities of observed PAN found in the
stratosphere between 13 and 14.5 km (Fig. 6e). In contrast, the black box stands for an air mass
where low pollution VMRs have been observed.

Fig. 9 gives an overview of the trajectory calculations. It is obvious that air masses were
365 transported by westerly winds to the place of GLORIA observations. If we first regard the black
box (as defined in Fig. 6) in the lowermost stratosphere, where low mixing ratios for all
pollutant species discussed here were observed, we find that only few trajectories penetrate the
upper planetary boundary layer (PBL) limit of 800 hPa on their way back from the GLORIA
observation points within 20-, 40-, and 60 days (Fig. 9a-c). Further, most of these areas are
370 located over the southern part of the North Pacific where we would not expect much pollution
in the PBL. In contrast, looking at the cyan and blues boxes (of Fig. 6) marking mainly air
masses in the upper troposphere near the flank of the stratospheric intrusion with generally high
amounts of the pollutants, we find lots of trajectories going into the PBL not only over the North
Pacific region but also over densely populated regions in Southeast Asia (Fig. 9d-i) where we
375 expect direct anthropogenic emissions or precursors of the considered species (Lelieveld et al.,



2001). Furthermore, marked areas of PBL penetration are also visible over the North American continent, especially in Canada where forest fires were frequent and intense in August and September 2017 (Pumphrey et al., 2020; Torres et al., 2020; Hooghiem et al., 2020; Khaykin et al., 2018). These widespread Canadian fires correlate well with the marked PBL areas. Finally, we look at the green region in the stratosphere around 14 km (see Fig. 6) where enhanced amounts of PAN are visible in contrast to the non-elevated values of C₂H₆, C₂H₂, and HCOOH. The corresponding trajectory calculations (Fig. 9j-l) exhibit no PBL penetration areas in the case of 20- and 40-days backward trajectories. However, the 60-days backward calculations clearly show areas over densely populated Southeast Asia where trajectories entered the PBL. The ascending air masses are clearly visible in the changing colour of the potential temperature along the trajectories (Fig. 9l). This potential source region is located well within the Asian summer monsoon pollution pump (Lelieveld et al., 2018; Randel et al., 2010). Since PAN has a lifetime of up to a few months in the free and upper troposphere which is longer than the one of C₂H₆, C₂H₂, and HCOOH, it is likely that some amounts of PAN are still existing in the stratospheric region of the green box while concentrations of the three other pollutant species are already depleted.

Backward trajectory calculations are very useful to identify both the origin of an air parcel in the PBL and its detailed transport pathways, however mixing processes between different air parcels are neglected. Therefore, we use in addition global three-dimensional CLaMS simulations considering mixing of air parcels to characterize the origin of air masses.

3.3.2 Artificial tracers of air mass origin calculations

The Lagrangian three-dimensional chemistry transport model CLaMS (Pommrich et al., 2014, and references therein) was used to calculate artificial tracers of air mass origin (Vogel et al., 2016; Vogel et al., 2019). These artificial tracers refer to marked geographical regions in the boundary layer of the global atmosphere. An overview of these regions is given in Fig. 10 which is an updated configuration compared to previous studies using artificial tracers of air mass origin in CLaMS. The upper limit of the model boundary layer follows the orography and extends to about 2-3 km above the Earth's surface. In the currently used simulation, the model dynamics is driven by horizontal winds from the ERA-interim reanalysis (Dee et al., 2011) provided by ECMWF. Transport of air masses from the model boundary into the free troposphere and above is considered from 1 May 2017, the starting time of the simulation. Every 24 h (time step for mixing in CLaMS), air masses in the model boundary layer are marked



by the different tracers of air mass origin and can be transported like a chemical tracer to other regions of the free troposphere or stratosphere and subsequent mixing processes between different air masses can occur. Therefore, the value of the individual artificial tracer of air mass origin counts the percentage of an air mass that originated in the specific model boundary layer region since 1 May 2017 considering advection and mixing processes.

The results of the CLaMS simulation are displayed in Fig. 11. The origin of air masses seen inside the cyan and blue boxes (which contain the largest values of C_2H_6 , C_2H_2 , $HCOOH$, and PAN, see Fig. 6) below the tropical side of the stratospheric intrusion stem to a large part from North America, the Northeast and Northwest Pacific and the Tropical Eastern Pacific; to a smaller part also from Central America. Up to about 40 % in these boxes originate from the South Asian region which includes Tibetan Plateau, Eastern China, Northern India, Indian Ocean, Bay of Bengal, Indian subcontinent, Southeast Asia, and Warm pool (see Fig. 10). This is consistent with the findings of the trajectory calculations as shown in the previous section. Air masses in the stratosphere within the green box where enhanced PAN mixing ratios were detected by GLORIA come mainly from the South Asian region. This is also in agreement with the PBL penetration region of the backward trajectories as discussed before. Concerning the black box in the stratosphere with low concentrations of C_2H_6 , C_2H_2 , $HCOOH$, and PAN, it is obvious that only fragments of air originate from the North American, Northeast and Northwest Pacific region. Some patches of South Asian air masses are visible in the black box zone, obviously from regions without enhanced amounts of the pollutants discussed here.

The artificial tracers of air mass origin mark specific geographical regions in the model boundary layer and are therefore very useful to identify the origin of observed air masses including atmospheric mixing processes. However, the real regions on the Earth's surface with high emissions of chemical tracers such as C_2H_6 , C_2H_2 , $HCOOH$, and PAN (or their precursors) are not included in the CLaMS simulations. Nevertheless, CLaMS simulations are useful to show that the enhanced PAN mixing ratios in the lower stratosphere (green box) are mainly from South Asia in agreement to the trajectory calculations.

435

4 Conclusions

GLORIA trace gas observations shown in this work were performed during a flight of the WISE aircraft campaign around the British Isles on 13 September 2017. The following main results can be stated:



440 First, enhanced volume mixing ratios of the pollutant gases C_2H_6 , C_2H_2 , $HCOOH$, and PAN
were recorded by the GLORIA instrument in the upper troposphere with high spatial resolution.
These enhancements were detected far away from the emission sources of these species. This
is possible due to their long atmospheric lifetimes in the order of weeks to months under free
tropospheric conditions. Since PAN has the longest lifetime of this foursome, elevated
445 quantities of this molecule could be measured even in the lowermost stratosphere. The main
sources of the emitted species are on the one hand biomass forest fires in North America which
reached their maximum a couple of weeks before the GLORIA flight (Pumphrey et al., 2020;
Torres et al., 2020) when air masses detected by GLORIA passed this region. On the other
hand, another important source region is located in the vast region of South and Southeast Asia
450 where the Asian monsoon anticyclone governs the circulation regime during the summer
months. Here, huge amounts of pollutants are lifted upwards into the upper troposphere and
further transported to northern midlatitudes via strong wind fields like the subtropical jet stream
(see, e.g., Lelieveld et al., 2018; Legras and Bucci, 2020). Indeed, another GLORIA
measurement carried out about 6 weeks earlier on 31 July 2017 during the StratoClim
455 (Stratospheric and upper tropospheric processes for better climate predictions) campaign over
India and Nepal also shows elevated amounts of more than 0.2 ppbv of C_2H_2 , more than 0.2
ppbv of $HCOOH$, and more than 0.5 ppbv of PAN (Johansson et al., 2020). These values are of
comparable magnitude to the ones observed during the WISE campaign.

Second, the chemistry climate model EMAC and the CAMS assimilation system are able to
460 simulate tropospheric and stratospheric dynamical ozone VMR structures as seen by GLORIA
although (primarily CAMS) with coarser spatial resolution compared to the measurement. In
addition, both models reproduce the temporal and spatial region of enhanced upper tropospheric
VMR levels of the measured pollutant species (C_2H_2 not available in CAMS). However, CAMS
clearly underestimates the amount of elevated C_2H_6 , $HCOOH$, and to a lesser extent, PAN. The
465 EMAC_2 simulation using NMVOC emissions enhanced by a factor of 2 (as recommended by
Monks et al., 2018) only slightly underestimates the C_2H_2 concentrations while simulated
values for C_2H_6 and $HCOOH$ are also too low. Compared to the EMAC standard emission run,
the EMAC_2 simulation reduces differences to the GLORIA observations for these gases. In
contrast, the size of elevated PAN values is overestimated by the EMAC_2 model run.
470 However, this does not hold for the local PAN VMR enhancements detected near 14 km, which
are neither captured by EMAC_2 nor by CAMS.



This study has shown that observations of pollutant species are further needed since biomass burning and wildfires will still occur in the future and seem to have increased in the last years (Witze, 2020). There is still potential to improve chemical models with regard to reproduce the measured VMR enhancements of the pollutant gases in more detail. One aspect is to improve the emission databases in the models because the simulated amount of pollution species is strongly dependent on the local emission place and the intensity of the emissions.

Data availability. GLORIA measurements are available in the database HALO-DB (<https://halo-db.pa.op.dlr.de/mission/96>) and will be available on the KITopen repository. The CAMS model data is available from ECMWF (<https://apps.ecmwf.int/data-catalogues/cams-reanalysis>). EMAC and CLaMS data are available upon request.

Author contributions. GW wrote the paper and performed the bulk of the data analysis, with input from all co-authors. SJ, AK, JU, MH, and NG performed the GLORIA data processing. FFV, TG, EK, GM, HN, and CP operated GLORIA during the WISE campaign in Shannon and Oberpfaffenhofen. OK and FK performed the EMAC simulations and designed the sensitivity studies. BV and JUG performed the CLaMS trajectory- and artificial tracers of air mass origin calculations. BMS, HO, and JO led the funding application and directed the flight planning and research. All authors commented on and improved the manuscript.

Competing interests. The authors declare that they have no conflict of interest.

Special issue statement. This article is part of the special issue “WISE: Wave-driven isentropic exchange in the extratropical upper stratosphere and lower stratosphere (ACP/AMT/WCD inter-journal SI), 2019”. It is not associated with a conference.

Acknowledgements. We acknowledge support by the German Research Foundation (Deutsche Forschungsgemeinschaft, DFG Priority Program SPP 1294). We are grateful to the WISE coordination team for excellently conducting the aircraft campaign. Results are based on the efforts of all members of the GLORIA team, including the technology institutes ZEA-1 and



ZEA-2 at Forschungszentrum Jülich and the Institute for Data Processing and Electronics at the Karlsruhe Institute of Technology. We would also like to thank the pilots and ground-support team at the Flight Experiments facility of the Deutsches Zentrum für Luft- und Raumfahrt 505 (DLR-FX). We thank ECMWF for providing CAMS data. The EMAC simulations were performed on the supercomputer ForHLR funded by the Ministry of Science, Research and the Arts Baden-Württemberg and by the Federal Ministry of Education and Research. The CLaMS activities contribute to the DFG project AMOS (HALO-SPP 1294/VO 1276/5-1) funded by the German Research Foundation (Deutsche Forschungsgemeinschaft, DFG). The authors 510 gratefully acknowledge the computing time for the CLaMS simulations granted on the supercomputer JURECA at Jülich Supercomputing Centre (JSC) under the VSR project ID JICG11.

Financial support. We acknowledge support by Deutsche Forschungsgemeinschaft and Open 515 Access Publishing Fund of Karlsruhe Institute of Technology.



References

- Alvarado, L. M. A., Richter, A., Vrekoussis, M., Hilboll, A., Kalisz Hedegaard, A. B.,
Schneising, O., and Burrows, J. P.: Unexpected long-range transport of glyoxal and
520 formaldehyde observed from the Copernicus Sentinel-5 Precursor satellite during the 2018
Canadian wildfires, *Atmos. Chem. Phys.*, 20, 2057–2072, <https://doi.org/10.5194/acp-20-2057-2020>, 2020.
- Atkinson, R., Baulch, D. L., Cox, R. A., Crowley, J. N., Hampson, R. F., Hynes, R. G.,
Jenkin, M. E., Rossi, M. J., and Troe, J.: Evaluated kinetic and photochemical data for
525 atmospheric chemistry: Volume III – gas phase reactions of inorganic halogens,
Atmos. Chem. Phys., 7, 981–1191, <https://doi.org/10.5194/acp-7-981-2007>, 2007.
- Brasseur, G. P. and Solomon, S.: *Aeronomy of the Middle Atmosphere: Chemistry and
Physics of the Stratosphere and Mesosphere*, Third revised and enlarged edition,
Atmospheric and Oceanographic Sciences Library, 32, Springer, Dordrecht, 2005.
- 530 Coheur, P.-F., Herbin, H., Clerbaux, C., Hurtmans, D., Wespes, C., Carleer, M., Turquety, S.,
Rinsland, C. P., Remedios, J., Hauglustaine, D., Boone, C. D., and Bernath, P. F.: ACE-
FTS observation of a young biomass burning plume: first reported measurements of C₂H₄,
C₃H₆O, H₂CO and PAN by infrared occultation from space, *Atmos. Chem. Phys.*, 7,
5437–5446, <https://doi.org/10.5194/acp-7-5437-2007>, 2007.
- 535 Cortesi, U., Lambert, J. C., Clercq, C. de, Bianchini, G., Blumenstock, T., Bracher, A.,
Castelli, E., Catoire, V., Chance, K. V., Mazière, M. de, Demoulin, P., Godin-Beekmann,
S., Jones, N., Jucks, K., Keim, C., Kerzenmacher, T., Kuellmann, H., Kuttippurath, J.,
Iarlori, M., Liu, G. Y., Liu, Y., McDermid, I. S., Meijer, Y. J., Mencaraglia, F., Mikuteit,
S., Oelhaf, H., Piccolo, C., Pirre, M., Raspollini, P., Ravegnani, F., Reburn, W. J.,
540 Redaelli, G., Remedios, J. J., Sembhi, H., Smale, D., Steck, T., Taddei, A., Varotsos, C.,
Vigouroux, C., Waterfall, A., Wetzell, G., and Wood, S.: Geophysical validation of
MIPAS-ENVISAT operational ozone data, *Atmos. Chem. Phys.*, 7, 4807–4867,
<https://doi.org/10.5194/acp-7-4807-2007>, 2007.
- Dee, D. P., Uppala, S. M., Simmons, A. J., Berrisford, P., Poli, P., Kobayashi, S., Andrae, U.,
545 Balmaseda, M. A., Balsamo, G., Bauer, P., Bechtold, P., Beljaars, A. C. M., van de Berg,
L., Bidlot, J., Bormann, N., Delsol, C., Dragani, R., Fuentes, M., Geer, A. J., Haimberger,
L., Healy, S. B., Hersbach, H., Hólm, E. V., Isaksen, L., Kållberg, P., Köhler, M.,



- 550 Matricardi, M., McNally, A. P., Monge-Sanz, B. M., Morcrette, J.-J., Park, B.-K., Peubey, C., Rosnay, P. de, Tavolato, C., Thépaut, J.-N., and Vitart, F.: The ERA-Interim reanalysis: configuration and performance of the data assimilation system, *Q.J.R. Meteorol. Soc.*, 137, 553–597, <https://doi.org/10.1002/qj.828>, 2011.
- 555 Fadnavis, S., Semeniuk, K., Schultz, M. G., Kiefer, M., Mahajan, A., Pozzoli, L., and Sonbawane, S.: Transport pathways of peroxyacetyl nitrate in the upper troposphere and lower stratosphere from different monsoon systems during the summer monsoon season, *Atmos. Chem. Phys.*, 15, 11477–11499, <https://doi.org/10.5194/acp-15-11477-2015>, 2015.
- 560 Fadnavis, S., Schultz, M. G., Semeniuk, K., Mahajan, A. S., Pozzoli, L., Sonbawane, S., Ghude, S. D., Kiefer, M., and Eckert, E.: Trends in peroxyacetyl nitrate (PAN) in the upper troposphere and lower stratosphere over southern Asia during the summer monsoon season: regional impacts, *Atmos. Chem. Phys.*, 14, 12725–12743, <https://doi.org/10.5194/acp-14-12725-2014>, 2014.
- Fischer, E. V., Jacob, D. J., Yantosca, R. M., Sulprizio, M. P., Millet, D. B., Mao, J., Paulot, F., Singh, H. B., Roiger, A., Ries, L., Talbot, R. W., Dzepina, K., and Pandey Deolal, S.: Atmospheric peroxyacetyl nitrate (PAN): a global budget and source attribution, *Atmos. Chem. Phys.*, 14, 2679–2698, <https://doi.org/10.5194/acp-14-2679-2014>, 2014.
- 565 Forster, P. M. d. F. and Shine, K. P.: Radiative forcing and temperature trends from stratospheric ozone changes, *J. Geophys. Res.*, 102, 10841–10855, <https://doi.org/10.1029/96JD03510>, 1997.
- 570 Friedl-Vallon, F., Gulde, T., Hase, F., Kleinert, A., Kulesa, T., Maucher, G., Neubert, T., Olschewski, F., Piesch, C., Preusse, P., Rongen, H., Sartorius, C., Schneider, H., Schönfeld, A., Tan, V., Bayer, N., Blank, J., Dapp, R., Ebersoldt, A., Fischer, H., Graf, F., Guggenmoser, T., Höpfner, M., Kaufmann, M., Kretschmer, E., Latzko, T., Nordmeyer, H., Oelhaf, H., Orphal, J., Riese, M., Schardt, G., Schillings, J., Sha, M. K., Suminska-Ebersoldt, O., and Ungermann, J.: Instrument concept of the imaging Fourier transform spectrometer GLORIA, *Atmos. Meas. Tech.*, 7, 3565–3577, <https://doi.org/10.5194/amt-7-3565-2014>, 2014.
- 575 Glatthor, N., Clarmann, T. von, Stiller, G. P., Funke, B., Koukouli, M. E., Fischer, H., Grabowski, U., Höpfner, M., Kellmann, S., and Linden, A.: Large-scale upper



- tropospheric pollution observed by MIPAS HCN and C₂H₆ global distributions, *Atmos. Chem. Phys.*, 9, 9619–9634, <https://doi.org/10.5194/acp-9-9619-2009>, 2009.
- 580 Gordon, I. E., Rothman, L. S., Hill, C., Kochanov, R. V., Tan, Y., Bernath, P. F., Birk, M.,
Boudon, V., Campargue, A., Chance, K. V., Drouin, B. J., Flaud, J.-M., Gamache, R. R.,
Hodges, J. T., Jacquemart, D., Perevalov, V. I., Perrin, A., Shine, K. P., Smith, M.-A.,
Tennyson, J., Toon, G. C., Tran, H., Tyuterev, V. G., Barbe, A., Császár, A. G., Devi, V.
M., Furtenbacher, T., Harrison, J. J., Hartmann, J.-M., Jolly, A., Johnson, T. J., Karman,
585 T., Kleiner, I., Kyuberis, A. A., Loos, J., Lyulin, O. M., Massie, S. T., Mikhailenko, S. N.,
Moazzen-Ahmadi, N., Müller, H., Naumenko, O. V., Nikitin, A. V., Polyansky, O. L.,
Rey, M., Rotger, M., Sharpe, S. W., Sung, K., Starikova, E., Tashkun, S. A., Auwera, J.
V., Wagner, G., Wilzewski, J., Wcisło, P., Yu, S., and Zak, E. J.: The HITRAN2016
molecular spectroscopic database, *Journal of Quantitative Spectroscopy and Radiative*
590 *Transfer*, 203, 3–69, <https://doi.org/10.1016/j.jqsrt.2017.06.038>, 2017.
- Granier, C., Bessagnet, B., Bond, T., D'Angiola, A., van der Denier Gon, H., Frost, G. J.,
Heil, A., Kaiser, J. W., Kinne, S., Klimont, Z., Kloster, S., Lamarque, J.-F., Liousse, C.,
Masui, T., Meleux, F., Mieville, A., Ohara, T., Raut, J.-C., Riahi, K., Schultz, M. G.,
Smith, S. J., Thompson, A., van Aardenne, J., van der Werf, G. R., and van Vuuren, D. P.:
595 Evolution of anthropogenic and biomass burning emissions of air pollutants at global and
regional scales during the 1980–2010 period, *Climatic Change*, 109, 163–190,
<https://doi.org/10.1007/s10584-011-0154-1>, 2011.
- Grutter, M., Glatthor, N., Stiller, G. P., Fischer, H., Grabowski, U., Höpfner, M., Kellmann,
S., Linden, A., and Clarmann, T. von: Global distribution and variability of formic acid as
600 observed by MIPAS-ENVISAT, *J. Geophys. Res.*, 115, 955,
<https://doi.org/10.1029/2009JD012980>, 2010.
- Hansen, J., Sato, M., and Ruedy, R.: Radiative forcing and climate response, *J. Geophys.*
Res., 102, 6831–6864, <https://doi.org/10.1029/96JD03436>, 1997.
- Hooghiem, J. J. D., Popa, M. E., Röckmann, T., Grooß, J.-U., Tritscher, I., Müller, R., Kivi,
605 R., and Chen, H.: Wildfire smoke in the lower stratosphere identified by in situ CO
observations, *Atmos. Chem. Phys. Discuss.*, 2020, 1–27, [https://doi.org/10.5194/acp-](https://doi.org/10.5194/acp-2020-65)
2020-65, available at: <https://acp.copernicus.org/preprints/acp-2020-65/>, 2020.



- Höpfner, M., Oelhaf, H., Wetzel, G., Friedl-Vallon, F., Kleinert, A., Lengel, A., Maucher, G., Nordmeyer, H., Glatthor, N., Stiller, G., Clarmann, T. v., Fischer, H., Kröger, C., and
610 Deshler, T.: Evidence of scattering of tropospheric radiation by PSCs in mid-IR limb emission spectra: MIPAS-B observations and KOPRA simulations, *Geophys. Res. Lett.*, 29, 119-1-119-4, <https://doi.org/10.1029/2001GL014443>, 2002.
- Inness, A., Ades, M., Agustí-Panareda, A., Barré, J., Benedictow, A., Blechschmidt, A.-M., Dominguez, J. J., Engelen, R., Eskes, H., Flemming, J., Huijnen, V., Jones, L., Kipling,
615 Z., Massart, S., Parrington, M., Peuch, V.-H., Razinger, M., Remy, S., Schulz, M., and Suttie, M.: The CAMS reanalysis of atmospheric composition, *Atmos. Chem. Phys.*, 19, 3515–3556, <https://doi.org/10.5194/acp-19-3515-2019>, 2019.
- Jöckel, P., Kerkweg, A., Pozzer, A., Sander, R., Tost, H., Riede, H., Baumgaertner, A., Gromov, S., and Kern, B.: Development cycle 2 of the Modular Earth Submodel System (MESSy2), *Geosci. Model Dev.*, 3, 717–752, <https://doi.org/10.5194/gmd-3-717-2010>,
620 2010.
- Johansson, S., Höpfner, M., Kirner, O., Wohltmann, I., Bucci, S., Legras, B., Friedl-Vallon, F., Glatthor, N., Kretschmer, E., Ungermann, J., and Wetzel, G.: Pollution trace gas distributions and their transport in the Asian monsoon upper troposphere and lowermost
625 stratosphere during the StratoClim campaign 2017, *Atmos. Chem. Phys.*, 20, 14695–14715, <https://doi.org/10.5194/acp-20-14695-2020>, 2020.
- Johansson, S., Woiwode, W., Höpfner, M., Friedl-Vallon, F., Kleinert, A., Kretschmer, E., Latzko, T., Orphal, J., Preusse, P., Ungermann, J., Santee, M. L., Jurkat-Witschas, T., Marsing, A., Voigt, C., Giez, A., Krämer, M., Rolf, C., Zahn, A., Engel, A., Sinnhuber,
630 B.-M., and Oelhaf, H.: Airborne limb-imaging measurements of temperature, HNO₃, O₃, ClONO₂, H₂O and CFC-12 during the Arctic winter 2015/2016: characterization, in situ validation and comparison to Aura/MLS, *Atmos. Meas. Tech.*, 11, 4737–4756, <https://doi.org/10.5194/amt-11-4737-2018>, 2018.
- Khare, P., Kumar, N., Kumari, K. M., and Srivastava, S. S.: Atmospheric formic and acetic
635 acids: An overview, *Rev. Geophys.*, 37, 227–248, <https://doi.org/10.1029/1998RG900005>, 1999.
- Khaykin, S. M., Godin-Beekmann, S., Hauchecorne, A., Pelon, J., Ravetta, F., and Keckhut, P.: Stratospheric smoke with unprecedentedly high backscatter observed by lidars above



- southern France, *Geophys. Res. Lett.*, 45, 1639–1646,
640 <https://doi.org/10.1002/2017GL076763>, 2018.
- Kleinert, A., Friedl-Vallon, F., Guggenmoser, T., Höpfner, M., Neubert, T., Ribalda, R., Sha, M. K., Ungermann, J., Blank, J., Ebersoldt, A., Kretschmer, E., Latzko, T., Oelhaf, H., Olschewski, F., and Preusse, P.: Level 0 to 1 processing of the imaging Fourier transform spectrometer GLORIA: generation of radiometrically and spectrally calibrated spectra,
645 *Atmos. Meas. Tech.*, 7, 4167–4184, <https://doi.org/10.5194/amt-7-4167-2014>, 2014.
- Lamarque, J.-F., Dentener, F., McConnell, J., Ro, C.-U., Shaw, M., Vet, R., Bergmann, D., Cameron-Smith, P., Dalsoren, S., Doherty, R., Faluvegi, G., Ghan, S. J., Josse, B., Lee, Y. H., MacKenzie, I. A., Plummer, D., Shindell, D. T., Skeie, R. B., Stevenson, D. S., Strode, S., Zeng, G., Curran, M., Dahl-Jensen, D., Das, S., Fritzsche, D., and Nolan, M.: Multi-
650 model mean nitrogen and sulfur deposition from the Atmospheric Chemistry and Climate Model Intercomparison Project (ACCMIP): evaluation of historical and projected future changes, *Atmos. Chem. Phys.*, 13, 7997–8018, <https://doi.org/10.5194/acp-13-7997-2013>, 2013.
- Legras, B. and Bucci, S.: Confinement of air in the Asian monsoon anticyclone and pathways
655 of convective air to the stratosphere during the summer season, *Atmos. Chem. Phys.*, 20, 11045–11064, <https://doi.org/10.5194/acp-20-11045-2020>, 2020.
- Lelieveld, J., Bourtsoukidis, E., Brühl, C., Fischer, H., Fuchs, H., Harder, H., Hofzumahaus, A., Holland, F., Marno, D., Neumaier, M., Pozzer, A., Schlager, H., Williams, J., Zahn, A., and Ziereis, H.: The South Asian monsoon-pollution pump and purifier, *Science (New York, N.Y.)*, 361, 270–273, <https://doi.org/10.1126/science.aar2501>, 2018.
660
- Lelieveld, J., Crutzen, P. J., Ramanathan, V., Andreae, M. O., Brenninkmeijer, C. M., Campos, T., Cass, G. R., Dickerson, R. R., Fischer, H., Gouw, J. A. de, Hansel, A., Jefferson, A., Kley, D., Laa, A. T. de, Lal, S., Lawrence, M. G., Lobert, J. M., Mayol-Bracero, O. L., Mitra, A. P., Novakov, T., Oltmans, S. J., Prather, K. A., Reiner, T.,
665 Rodhe, H., Scheeren, H. A., Sikka, D., and Williams, J.: The Indian Ocean experiment: widespread air pollution from South and Southeast Asia, *Science*, 291, 1031–1036, <https://doi.org/10.1126/science.1057103>, available at: <https://science.sciencemag.org/content/291/5506/1031/tab-pdf>, 2001.



- Li, D., Vogel, B., Müller, R., Bian, J., Günther, G., Li, Q., Zhang, J., Bai, Z., Vömel, H., and
670 Riese, M.: High tropospheric ozone in Lhasa within the Asian summer monsoon
anticyclone in 2013: influence of convective transport and stratospheric intrusions, *Atmos.*
Chem. Phys., 18, 17979–17994, <https://doi.org/10.5194/acp-18-17979-2018>, 2018.
- Livesey, N. J., Filipiak, M. J., Froidevaux, L., Read, W. G., Lambert, A., Santee, M. L., Jiang,
J. H., Pumphrey, H. C., Waters, J. W., Cofield, R. E., Cuddy, D. T., Daffer, W. H.,
675 Drouin, B. J., Fuller, R. A., Jarnot, R. F., Jiang, Y. B., Knosp, B. W., Li, Q. B., Perun, V.
S., Schwartz, M. J., Snyder, W. V., Stek, P. C., Thurstans, R. P., Wagner, P. A., Avery,
M., Browell, E. V., Cammas, J.-P., Christensen, L. E., Diskin, G. S., Gao, R.-S., Jost, H.-
J., Loewenstein, M., Lopez, J. D., Nedelec, P., Osterman, G. B., Sachse, G. W., and
Webster, C. R.: Validation of Aura Microwave Limb Sounder O₃ and CO observations in
680 the upper troposphere and lower stratosphere, *J. Geophys. Res.*, 113,
<https://doi.org/10.1029/2007JD008805>, 2008.
- Lu, X., Zhang, L., and Shen, L.: Meteorology and Climate Influences on Tropospheric Ozone:
a Review of Natural Sources, Chemistry, and Transport Patterns, *Curr Pollution Rep.*, 5,
238–260, <https://doi.org/10.1007/S40726-019-00118-3>, 2019.
- 685 McKenna, D. S., Konopka, P., Groß, J.-U., Günther, G., Müller, R., Spang, R., Offermann,
D., and Orsolini, Y.: A new Chemical Lagrangian Model of the Stratosphere (CLaMS) 1.
Formulation of advection and mixing, *J. Geophys. Res.*, 107,
<https://doi.org/10.1029/2000JD000114>, 2002a.
- McKenna, D. S., Groß, J.-U., Günther, G., Konopka, P., Müller, R., Carver, G., and Sasano,
690 Y.: A new Chemical Lagrangian Model of the Stratosphere (CLaMS) 2. Formulation of
chemistry scheme and initialization, *J. Geophys. Res.*, 107,
<https://doi.org/10.1029/2000JD000113>, 2002b.
- Millet, D. B., Baasandorj, M., Farmer, D. K., Thornton, J. A., Baumann, K., Brophy, P.,
Chaliyakunnel, S., Gouw, J. A. de, Graus, M., Hu, L., Koss, A., Lee, B. H., Lopez-
695 Hilfiker, F. D., Neuman, J. A., Paulot, F., Peischl, J., Pollack, I. B., Ryerson, T. B.,
Warneke, C., Williams, B. J., and Xu, J.: A large and ubiquitous source of atmospheric
formic acid, *Atmos. Chem. Phys.*, 15, 6283–6304, [https://doi.org/10.5194/acp-15-6283-](https://doi.org/10.5194/acp-15-6283-2015)
2015, 2015.



- Monks, S. A., Wilson, C., Emmons, L. K., Hannigan, J. W., Helmig, D., Blake, N. J., and
700 Blake, D. R.: Using an Inverse Model to Reconcile Differences in Simulated and
Observed Global Ethane Concentrations and Trends Between 2008 and 2014, *J. Geophys.
Res. Atmos.*, 123, 11,262–11,282, <https://doi.org/10.1029/2017JD028112>, 2018.
- Montzka, S. A., Butler, J. H., Elkins, J. W., Thompson, T. M., Clarke, A. D., and Lock, L. T.:
705 Present and future trends in the atmospheric burden of ozone-depleting halogens, *Nature*,
398, 690–694, <https://doi.org/10.1038/19499>, 1999.
- Mungall, E. L., Abbatt, J. P. D., Wentzell, J. J. B., Wentworth, G. R., Murphy, J. G., Kunkel,
D., Gute, E., Tarasick, D. W., Sharma, S., Cox, C. J., Uttal, T., and Liggio, J.: High gas-
phase mixing ratios of formic and acetic acid in the High Arctic, *Atmos. Chem. Phys.*, 18,
10237–10254, <https://doi.org/10.5194/acp-18-10237-2018>, 2018.
- 710 Norton, R. H. and Beer, R.: New apodizing functions for Fourier spectrometry, *J. Opt. Soc.
Am.*, 66, 259, <https://doi.org/10.1364/JOSA.66.000259>, 1976.
- Paulot, F., Wunch, D., Crouse, J. D., Toon, G. C., Millet, D. B., DeCarlo, P. F., Vigouroux,
C., Deutscher, N. M., González Abad, G., Notholt, J., Warneke, T., Hannigan, J. W.,
Warneke, C., Gouw, J. A. de, Dunlea, E. J., Mazière, M. de, Griffith, D. W. T., Bernath,
715 P., Jimenez, J. L., and Wennberg, P. O.: Importance of secondary sources in the
atmospheric budgets of formic and acetic acids, *Atmos. Chem. Phys.*, 11, 1989–2013,
<https://doi.org/10.5194/acp-11-1989-2011>, 2011.
- Phillips, D. L.: A technique for the numerical solution of certain integral equations of the first
kind, *J. Assoc. Comput. Math.*, 9, 84–97, <https://doi.org/10.1145/321105.321114>, 1962.
- 720 Ploeger, F., Konopka, P., Müller, R., Fueglistaler, S., Schmidt, T., Manners, J. C., Groöß, J.-
U., Günther, G., Forster, P. M., and Riese, M.: Horizontal transport affecting trace gas
seasonality in the Tropical Tropopause Layer (TTL), *J. Geophys. Res.*, 117, n/a-n/a,
<https://doi.org/10.1029/2011JD017267>, 2012.
- Pommrich, R., Müller, R., Groöß, J.-U., Konopka, P., Ploeger, F., Vogel, B., Tao, M., Hoppe,
725 C. M., Günther, G., Spelten, N., Hoffmann, L., Pumphrey, H.-C., Viciani, S., D'Amato, F.,
Volk, C. M., Hoor, P., Schlager, H., and Riese, M.: Tropical troposphere to stratosphere
transport of carbon monoxide and long-lived trace species in the Chemical Lagrangian
Model of the Stratosphere (CLaMS), *Geosci. Model Dev.*, 7, 2895–2916,
<https://doi.org/10.5194/gmd-7-2895-2014>, 2014.



- 730 Pumphrey, H. C., Schwartz, M. J., Santee, M. L., Kablick III, G. P., Fromm, M. D., and Livesey, N. J.: Stratospheric pollution from Canadian forest fires, 2020.
- Randel, W. J., Park, M., Emmons, L., Kinnison, D., Bernath, P., Walker, K. A., Boone, C., and Pumphrey, H.: Asian monsoon transport of pollution to the stratosphere, *Science* (New York, N.Y.), 328, 611–613, <https://doi.org/10.1126/science.1182274>, 2010.
- 735 Remedios, J. J., Leigh, R. J., Waterfall, A. M., Moore, D. P., Sembhi, H., Parkes, I., Greenhough, J., Chipperfield, M. P., and Hauglustaine, D.: MIPAS reference atmospheres and comparisons to V4.61/V4.62 MIPAS level 2 geophysical data sets, *Atmos. Chem. Phys. Discuss.*, 7, 9973–10017, <https://doi.org/10.5194/acpd-7-9973-2007>, 2007.
- Riese, M., Oelhaf, H., Preusse, P., Blank, J., Ern, M., Friedl-Vallon, F., Fischer, H.,
740 Guggenmoser, T., Höpfner, M., Hoor, P., Kaufmann, M., Orphal, J., Plöger, F., Spang, R., Suminska-Ebersoldt, O., Ungermann, J., Vogel, B., and Woiwode, W.: Gimballed Limb Observer for Radiance Imaging of the Atmosphere (GLORIA) scientific objectives, *Atmos. Meas. Tech.*, 7, 1915–1928, <https://doi.org/10.5194/amt-7-1915-2014>, 2014.
- Riese, M., Ploeger, F., Rap, A., Vogel, B., Konopka, P., Dameris, M., and Forster, P.: Impact
745 of uncertainties in atmospheric mixing on simulated UTLS composition and related radiative effects, *J. Geophys. Res.*, 117, n/a-n/a, <https://doi.org/10.1029/2012JD017751>, 2012.
- Rinsland, C. P., Boone, C. D., Bernath, P. F., Mahieu, E., Zander, R., Dufour, G., Clerbaux, C., Turquety, S., Chiou, L., McConnell, J. C., Neary, L., and Kaminski, J. W.: First space-
750 based observations of formic acid (HCOOH): Atmospheric Chemistry Experiment austral spring 2004 and 2005 Southern Hemisphere tropical-mid-latitude upper tropospheric measurements, *Geophys. Res. Lett.*, 33, 955, <https://doi.org/10.1029/2006GL027128>, 2006.
- Rinsland, C. P., Dufour, G., Boone, C. D., Bernath, P. F., and Chiou, L.: Atmospheric
755 Chemistry Experiment (ACE) measurements of elevated Southern Hemisphere upper tropospheric CO, C₂H₆, HCN, and C₂H₂ mixing ratios from biomass burning emissions and long-range transport, *Geophys. Res. Lett.*, 32, 24043, <https://doi.org/10.1029/2005GL024214>, 2005.
- Rodgers, C. D.: *Inverse methods for atmospheric sounding*, 2, World Sci., 2000.



- 760 Roeckner, E., Brokopf, R., Esch, M., Giorgetta, M., Hagemann, S., Kornbluh, L., Manzini, E., Schlese, U., and Schulzweida, U.: Sensitivity of Simulated Climate to Horizontal and Vertical Resolution in the ECHAM5 Atmosphere Model, *J. Climate*, 19, 3771–3791, <https://doi.org/10.1175/JCLI3824.1>, 2006.
- Rudolph, J.: The tropospheric distribution and budget of ethane, *J. Geophys. Res.*, 100, 765 11369, <https://doi.org/10.1029/95JD00693>, 1995.
- Sander, S. P., Friedl, R. R., Barker, J. R., Golden, D. M., Kurylo, M. J., Wine, P. H., Abbatt, J. P. D., Burkholder, J. B., Kolb, C. E., Moortgat, G. K., Huie, R. E., and Orkin, V. L.: Chemical kinetics and photochemical data for use in atmospheric studies, Evaluation no. 17, JPL Publ. 10-6, Jet Propulsion Laboratory, Pasadena, CA, 2011.
- 770 Singh, H., Chen, Y., Staudt, A., Jacob, D., Blake, D., Heikes, B., and Snow, J.: Evidence from the Pacific troposphere for large global sources of oxygenated organic compounds, *Nature*, 410, 1078–1081, <https://doi.org/10.1038/35074067>, 2001.
- Singh, H. B.: Reactive nitrogen in the troposphere, *Environ. Sci. Technol.*, 21, 320–327, <https://doi.org/10.1021/es00158a001>, 1987.
- 775 Spang, R., Remedios, J., and Barkley, M.: Colour indices for the detection and differentiation of cloud types in infra-red limb emission spectra, *Advances in Space Research*, 33, 1041–1047, [https://doi.org/10.1016/S0273-1177\(03\)00585-4](https://doi.org/10.1016/S0273-1177(03)00585-4), 2004.
- Stiller, G. P., Clarmann, T. von, Funke, B., Glatthor, N., Hase, F., Höpfner, M., and Linden, A.: Sensitivity of trace gas abundances retrievals from infrared limb emission spectra to 780 simplifying approximations in radiative transfer modelling, *Journal of Quantitative Spectroscopy and Radiative Transfer*, 72, 249–280, [https://doi.org/10.1016/S0022-4073\(01\)00123-6](https://doi.org/10.1016/S0022-4073(01)00123-6), 2002.
- Tikhonov, A. N.: On the solution of ill-posed problems and the method of regularization, *Dokl. Acad. Nauk SSSR*, 151, 501–504, 1963.
- 785 Torres, O., Bhartia, P. K., Taha, G., Jethva, H., Das, S., Colarco, P., Krotkov, N., Omar, A., and Ahn, C.: Stratospheric Injection of Massive Smoke Plume From Canadian Boreal Fires in 2017 as Seen by DSCOVR-EPIC, CALIOP, and OMPS-LP Observations, *J. Geophys. Res. Atmos.*, 125, <https://doi.org/10.1029/2020JD032579>, 2020.



- Ungermann, J., Ern, M., Kaufmann, M., Müller, R., Spang, R., Ploeger, F., Vogel, B., and
790 Riese, M.: Observations of PAN and its confinement in the Asian summer monsoon
anticyclone in high spatial resolution, *Atmos. Chem. Phys.*, 16, 8389–8403,
<https://doi.org/10.5194/acp-16-8389-2016>, 2016.
- Vogel, B., Günther, G., Müller, R., Groß, J.-U., Hoor, P., Krämer, M., Müller, S., Zahn, A.,
795 and Riese, M.: Fast transport from Southeast Asia boundary layer sources to northern
Europe: rapid uplift in typhoons and eastward eddy shedding of the Asian monsoon
anticyclone, *Atmos. Chem. Phys.*, 14, 12745–12762, <https://doi.org/10.5194/acp-14-12745-2014>, 2014.
- Vogel, B., Müller, R., Günther, G., Spang, R., Hanumanthu, S., Li, D., Riese, M., and Stiller,
800 G. P.: Lagrangian simulations of the transport of young air masses to the top of the Asian
monsoon anticyclone and into the tropical pipe, *Atmos. Chem. Phys.*, 19, 6007–6034,
<https://doi.org/10.5194/acp-19-6007-2019>, 2019.
- Vogel, B., Günther, G., Müller, R., Groß, J.-U., Afchine, A., Bozem, H., Hoor, P., Krämer,
M., Müller, S., Riese, M., Rolf, C., Spelten, N., Stiller, G. P., Ungermann, J., and Zahn,
805 A.: Long-range transport pathways of tropospheric source gases originating in Asia into
the northern lower stratosphere during the Asian monsoon season 2012, *Atmos. Chem.
Phys.*, 16, 15301–15325, <https://doi.org/10.5194/acp-16-15301-2016>, 2016.
- Wang, Y., Ma, Y.-F., Eskes, H., Inness, A., Flemming, J., and Brasseur, G. P.: Evaluation of
the CAMS global atmospheric trace gas reanalysis 2003-2016 using aircraft campaign
810 observations, *Atmos. Chem. Phys.*, 20, 4493–4521, <https://doi.org/10.5194/acp-20-4493-2020>, 2020.
- Wiegele, A., Glatthor, N., Höpfner, M., Grabowski, U., Kellmann, S., Linden, A., Stiller, G.,
and Clarmann, T. von: Global distributions of C₂H₆, C₂H₂, HCN, and PAN retrieved from
MIPAS reduced spectral resolution measurements, *Atmos. Meas. Tech.*, 5, 723–734,
<https://doi.org/10.5194/amt-5-723-2012>, 2012.
- 815 Witze, A.: The Arctic is burning like never before - and that's bad news for climate change,
Nature, 585, 336–337, <https://doi.org/10.1038/d41586-020-02568-y>, 2020.
- Xiao, Y., Logan, J. A., Jacob, D. J., Hudman, R. C., Yantosca, R., and Blake, D. R.: Global
budget of ethane and regional constraints on U.S. sources, *J. Geophys. Res.*, 113, 955,
<https://doi.org/10.1029/2007JD009415>, 2008.



- 820 Xiao, Y., Jacob, D. J., and Turquety, S.: Atmospheric acetylene and its relationship with CO
as an indicator of air mass age, *J. Geophys. Res.*, 112, 955,
<https://doi.org/10.1029/2006JD008268>, 2007.
- Xie, F., Tian, W., and Chipperfield, M. P.: Radiative effect of ozone change on stratosphere-
troposphere exchange, *J. Geophys. Res.*, 113, <https://doi.org/10.1029/2008JD009829>,
825 2008.
- Yuan, B., Veres, P. R., Warneke, C., Roberts, J. M., Gilman, J. B., Koss, A., Edwards, P. M.,
Graus, M., Kuster, W. C., Li, S.-M., Wild, R. J., Brown, S. S., Dubé, W. P., Lerner, B. M.,
Williams, E. J., Johnson, J. E., Quinn, P. K., Bates, T. S., Lefer, B., Hayes, P. L., Jimenez,
J. L., Weber, R. J., Zamora, R., Ervens, B., Millet, D. B., Rappenglück, B., and Gouw, J.
830 A. de: Investigation of secondary formation of formic acid: urban environment vs. oil and
gas producing region, *Atmos. Chem. Phys.*, 15, 1975–1993, <https://doi.org/10.5194/acp-15-1975-2015>, 2015.

835

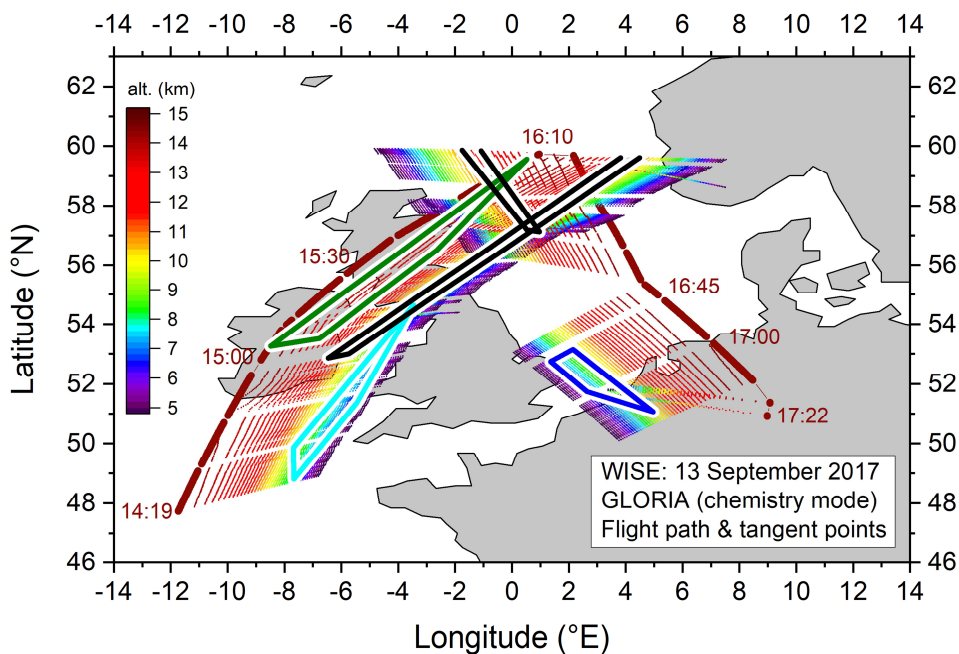


Figure 1. Path of the HALO flight on 13 September 2017 during the WISE campaign (large dark brown points) together with GLORIA tangent points (small points with changing colour according to altitude). Measurement times are given in UTC. Coloured framed zones mark areas of special interest as discussed in Sect. 3. Note that only observations performed in the chemistry mode are shown.

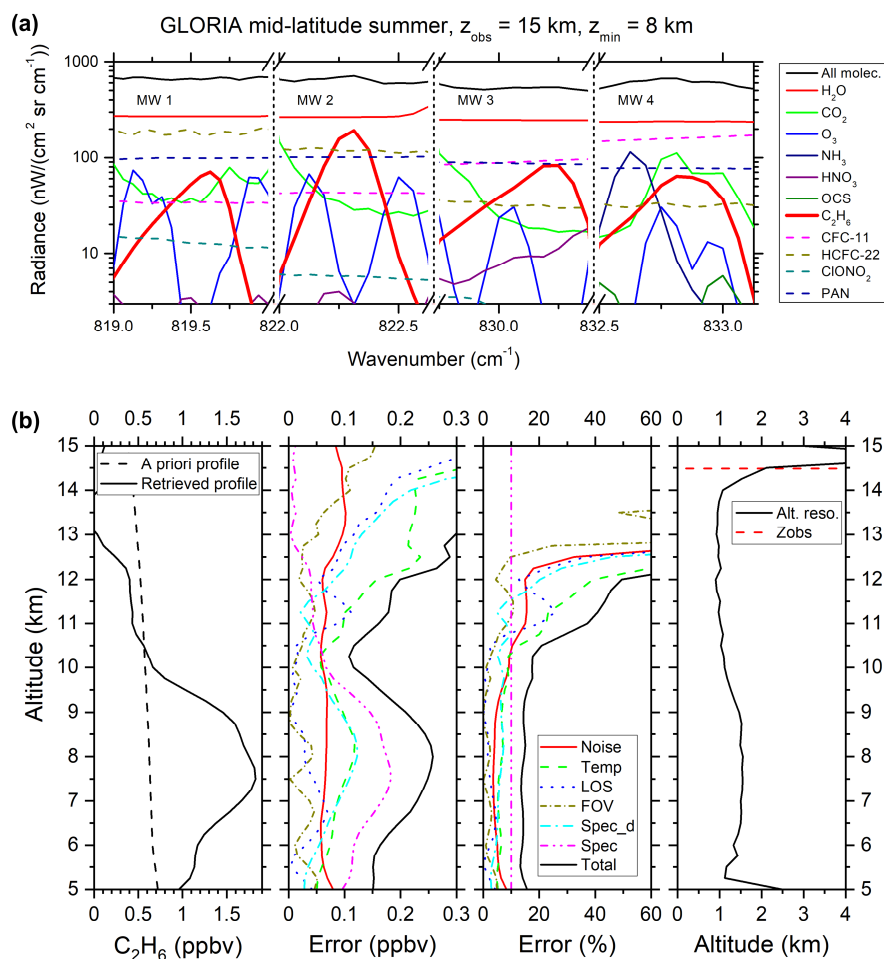


Figure 2. Simulated limb emission spectra (with spectral resolution of GLORIA) for a mid-latitude summer standard atmosphere (Remedios et al., 2007) in four microwindows in the spectral region of the C_2H_6 ν_9 band centred at 822 cm^{-1} for a tangent altitude of 8 km . Emissions of individual species contributing to the combined spectrum (all molecules, black line) are shown (a). Retrieved C_2H_6 VMR vertical profile (and a priori profile) of the limb sequence measured at 13 September 2017 at 16:55 UTC combined with absolute and relative errors and the altitude resolution (alt. reso.), determined from the full width at half maximum of the columns of the averaging kernel matrix, together with the observer altitude (z_{obs}). The following individual 1σ errors are shown: spectral noise (red solid line), temperature (green dashed line), line of sight (LOS; blue dotted line), field of view (FOV; dark yellow short dash dotted line) spectroscopic data of disturbing gases (cyan dash dotted line), spectroscopic data of target molecule C_2H_6 (dash dotted magenta line), and total error (black solid line) (b).

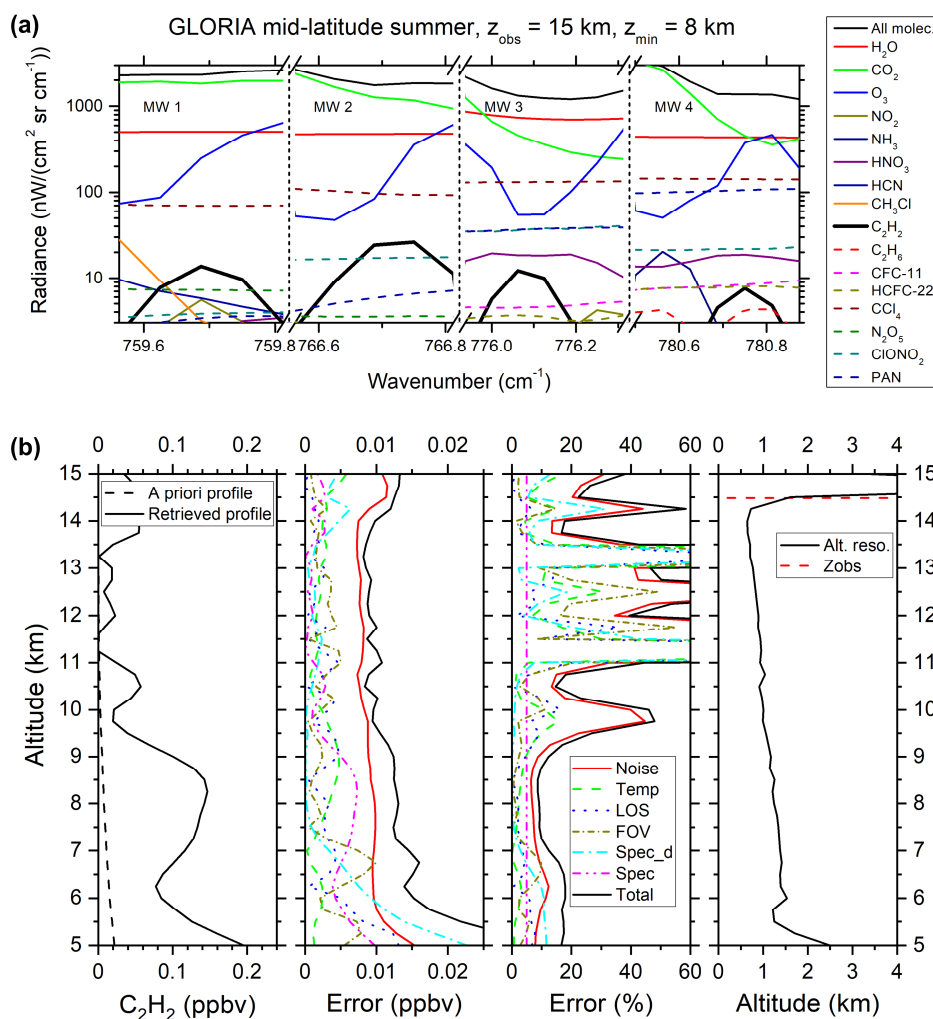


Figure 3. Simulated limb emission spectra for four microwindows within the C_2H_2 ν_5 band centred at 730 cm^{-1} for a tangent altitude of 8 km (a) and the error budget for a C_2H_2 vertical profile obtained on 13 September 2017 at 16:55 UTC (b). Annotation as per Fig. 2.

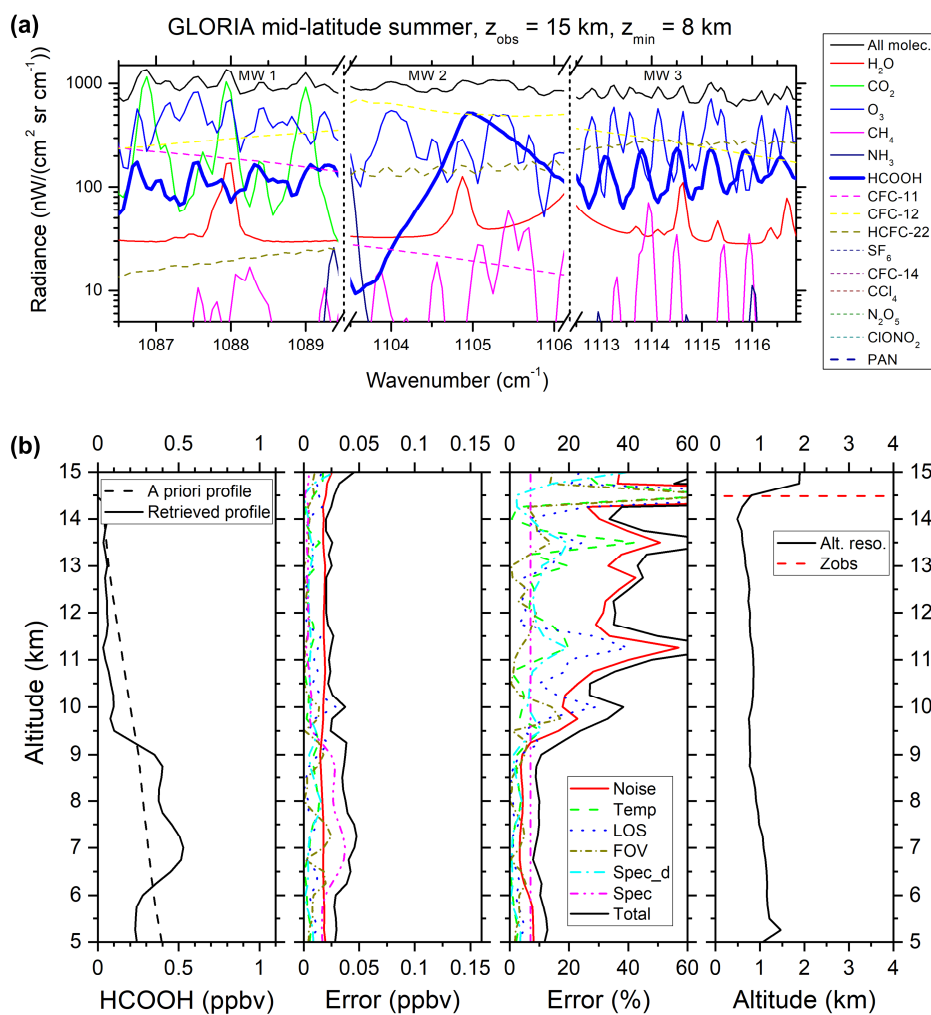


Figure 4. Simulated limb emission spectra for three microwindows within the HCOOH ν_6 band centred near 1105 cm^{-1} for a tangent altitude of 8 km **(a)** and the error budget for a HCOOH vertical profile obtained on 13 September 2017 at 16:55 UTC **(b)**. Annotation as per Fig. 2.

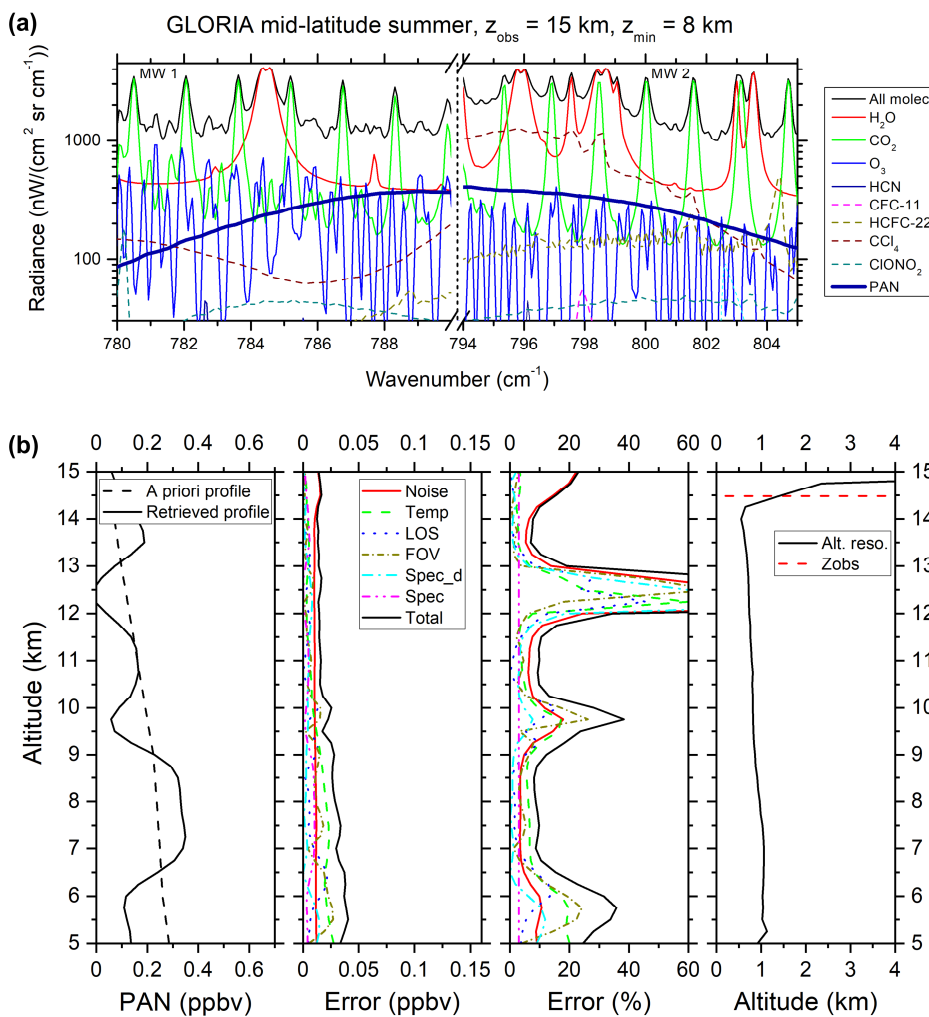


Figure 5. Simulated limb emission spectra for two microwindows within the PAN ν_{16} band centred near 792 cm^{-1} for a tangent altitude of 8 km (a) and the error budget for a PAN vertical profile obtained on 13 September 2017 at 16:55 UTC (b). Annotation as per Fig. 2.

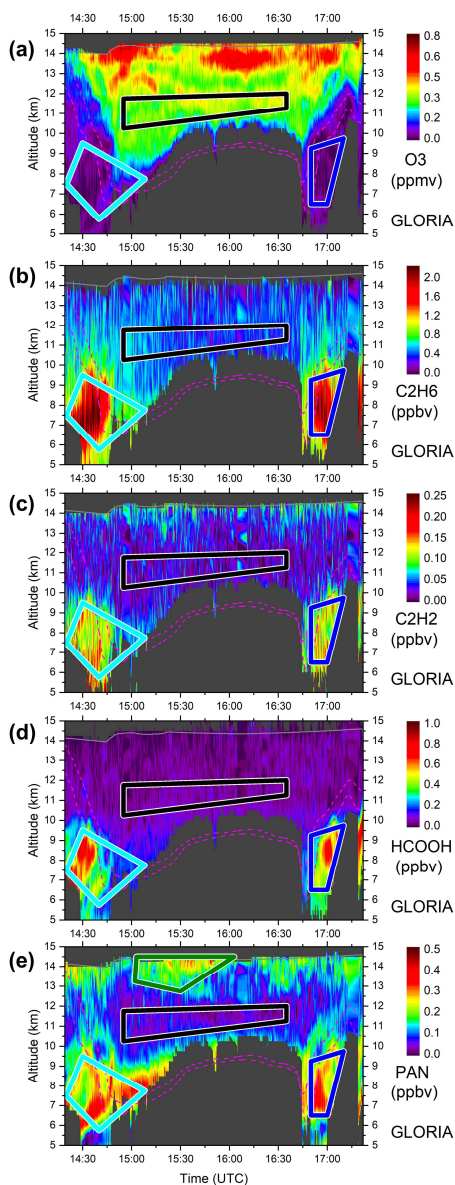


Figure 6. Horizontal and vertical VMR distributions of (a) O₃, (b) C₂H₆, (c) C₂H₂, (d) HCOOH, (e) PAN as seen by GLORIA above the North Atlantic region on 13 September 2017. Flight altitude is shown as grey line; dynamical tropopause (2 and 4 potential vorticity units from ECMWF) is plotted as dashed magenta lines. Cyan, blue and green (only PAN) coloured boxes mark regions with enhanced VMR levels, black boxes comprise a region with low mixing ratios. For all these boxes backward trajectories are calculated (see discussion in Sect. 3).

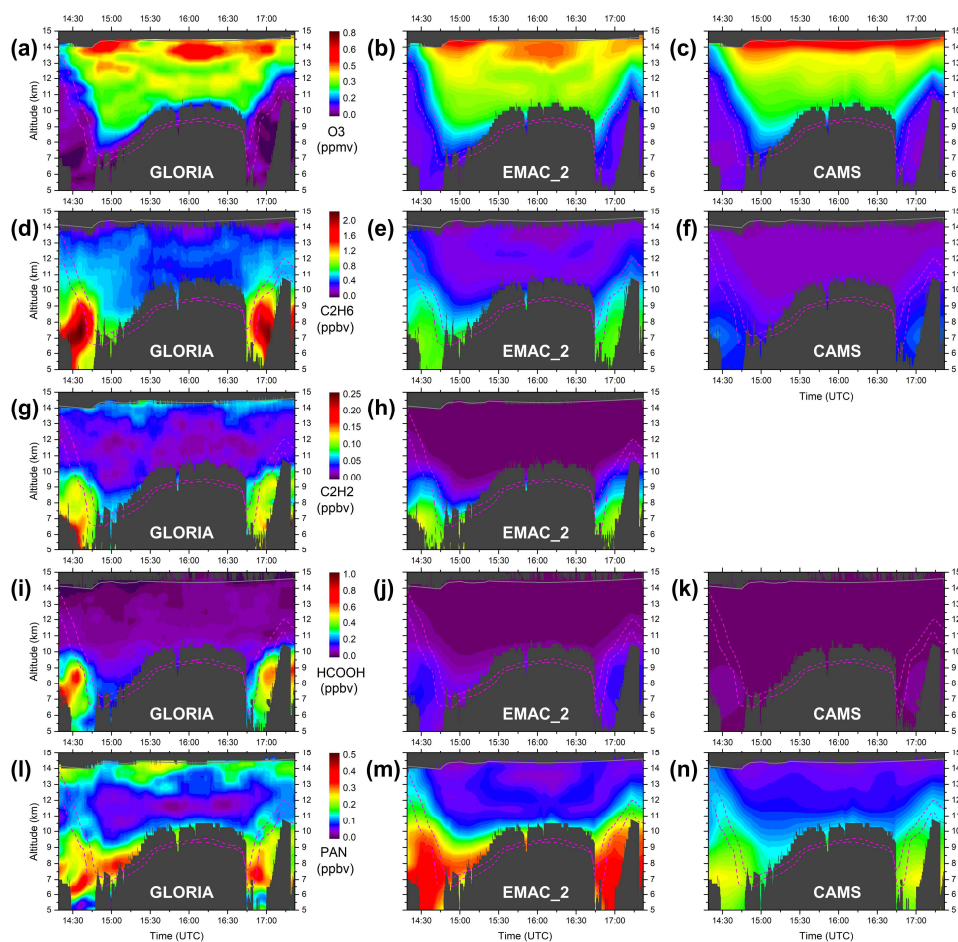


Figure 7. Horizontal and vertical VMR distributions of GLORIA (temporally smoothed, left column), EMAC_2 (middle column), and CAMS (right column) of (a-c) O₃, (d-f) C₂H₆, (g-h) C₂H₂, (i-k) HCOOH, and (l-n) PAN, as seen on 13 September 2017. The EMAC_2 simulation includes NMVOC emissions enhanced by a factor of 2 as recommended by Monks et al. (2018). No CAMS data for C₂H₂ is available. Annotation as per Fig. 6.

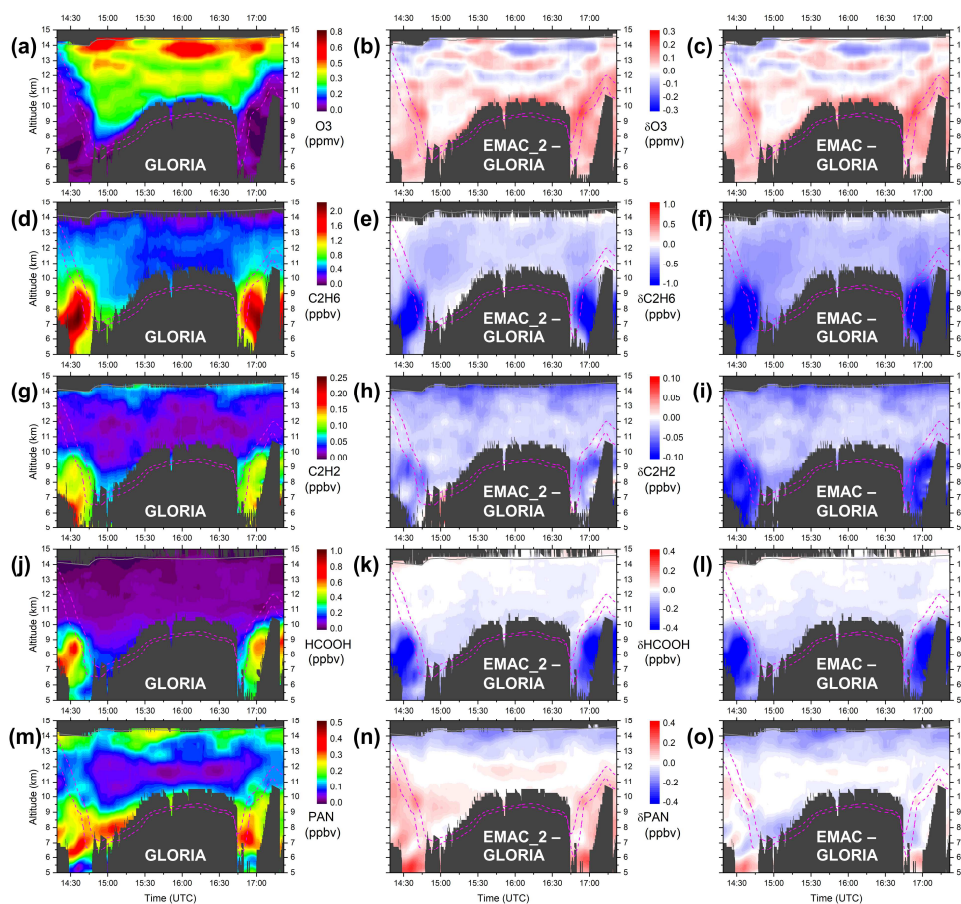


Figure 8. Horizontal and vertical VMR distributions of GLORIA (temporally smoothed, left column), EMAC_2 (enhanced NMVOC emissions) minus GLORIA (middle column), and EMAC (standard NMVOC emissions) minus GLORIA (right column) of (a-c) O₃, (d-f) C₂H₆, (g-i) C₂H₂, (j-l) HCOOH, and (m-o) PAN, as seen on 13 September 2017. Annotation as per Fig. 6.

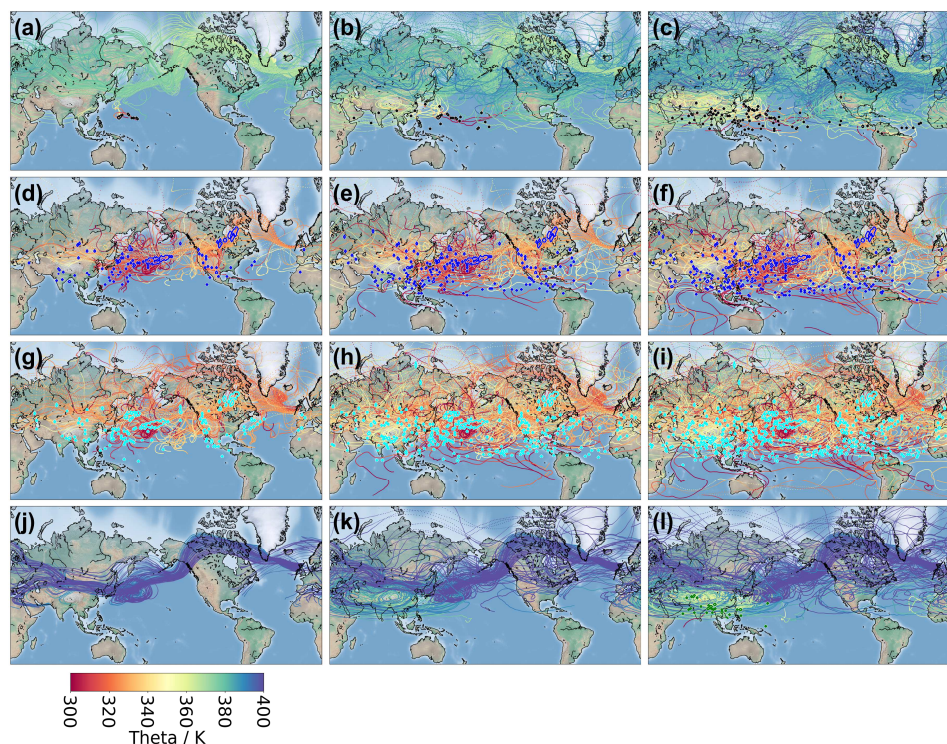


Figure 9. Backward trajectory calculations performed by CLaMS using ERA-interim wind data. Trajectories start at the GLORIA tangent points and are shown for 20 days (left column), 40 days
855 (middle column), and 60 days (right column) within defined regions: black (a-c), blue (d-f), cyan (g-i), and green (j-l) as displayed in Fig. 6. Trajectory colours denote the potential temperature (which is also a measure of altitude) along the trajectory as indicated in the colour bar. Coloured encircled areas mark regions where the backward trajectory penetrates the upper edge of the planetary boundary layer (800 hPa). For better clarity, only every tenth trajectory is displayed. Hence, encircled areas may occur where
860 no trajectory is drawn.

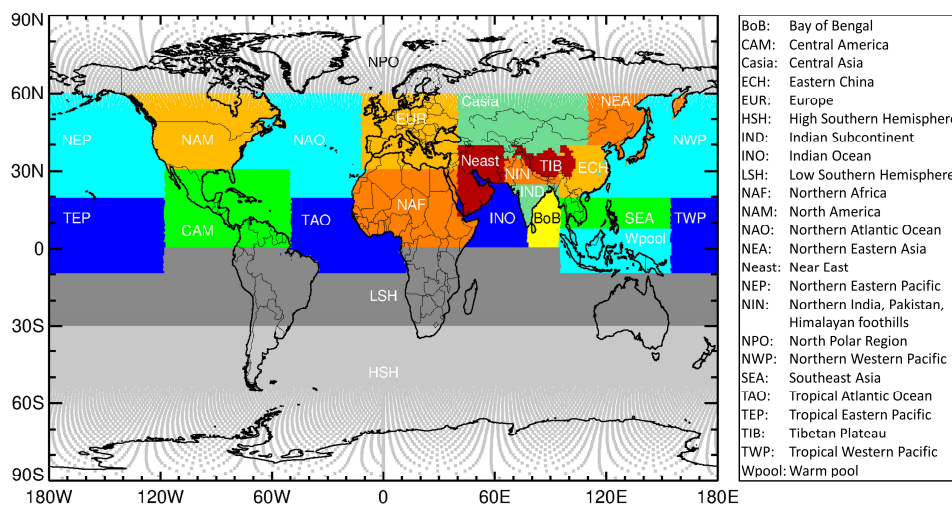
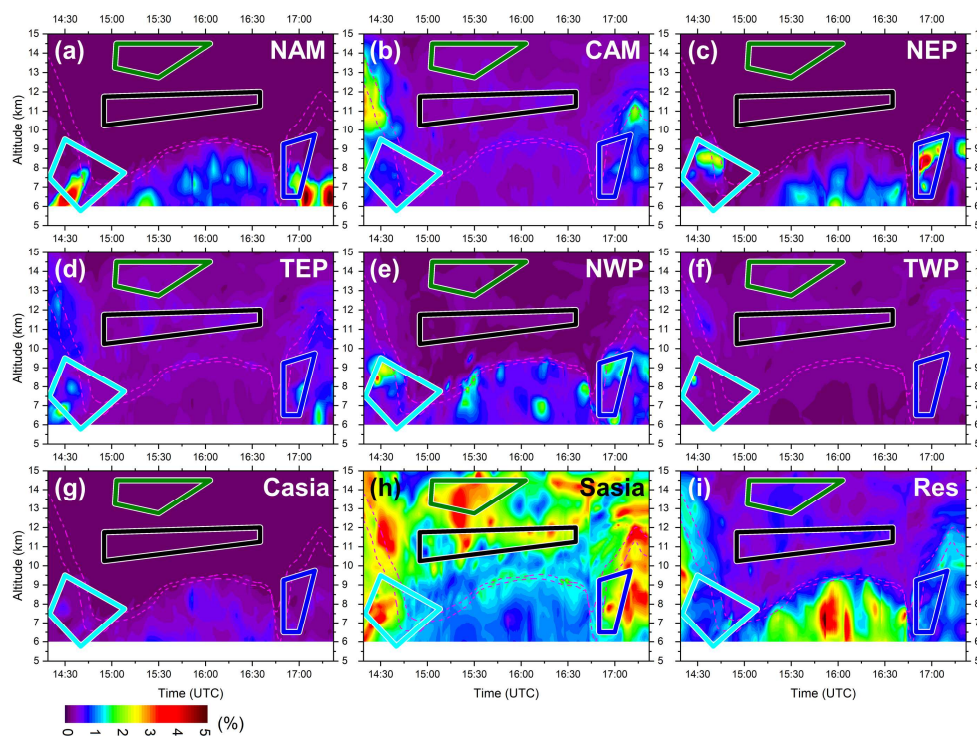


Figure 10. Geographical locations of the artificial tracers of air mass origin used in the CLaMS model for the HALO WISE campaign 2017. In some regions, the artificial tracers are defined to separate between continental and maritime areas as well as by different geopotential heights (e.g. Tibetan Plateau). The geographical locations of the artificial tracers of air mass origin used in previous CLaMS simulations can be found in Vogel et al. (2019).



865

Figure 11. Artificial tracers of air mass origin calculations performed with CLaMS for the GLORIA observation grid showing the horizontal and vertical distribution of fraction of air originating from the boundary layer of different geographical regions as defined in Fig. 10. Results are shown for zones from the North and Central American and Pacific region (**a-f**) and zones for Central Asia (**g**) and South Asia (Sasia) which comprises the subregions INO, IND, NIN, TIB, ECH, BoB, SEA, and Wpool (**g**). The residual part (Res) displayed in (**i**) includes all global regions except the zones shown in (**a-h**) and is of little importance for the GLORIA observations. Annotations as per Fig. 6.

870